Stalls and Splines: Current Trends in Flight Testing and Aerodynamic Model Identification

de Visser, C.C.; Pool, D.M.

DOI
10.2514/1.C037283

Publication date
2023

Document Version
Final published version

Published in
Journal of Aircraft: devoted to aeronautical science and technology

JOURNAL OF AIRCRAFT
Vol. 60, No. 5, September–October 2023

Stalls and Splines: Current Trends in Flight Testing and Aerodynamic Model Identification

Coen C. de Visser* and Daan M. Pool†
Delft University of Technology, 2600 GB Delft, The Netherlands

https://doi.org/10.2514/1.C037283

Aerodynamic model identification remains essential for simulator operations and control system design and operations. In this paper, state-of-the-art methodologies for aerodynamic model identification and validation are presented, together with a number of novel applications of the identified models that were recently investigated and developed at the Faculty of Aerospace Engineering of Delft University of Technology. In particular, this paper focuses on methodologies for identifying models of aerodynamic stall from flight data, as well as multivariate spline-based aerodynamic model identification methods, together with their applications in flight simulation and advanced flight control.

Nomenclature

A	=	matrix of regression variables
A_*	=	specific force in $*$ direction, m/s^2
$\boldsymbol{a}$	=	regression variable vector
a_1	=	X parameter for shape
$\boldsymbol{B}^d_{t_j}(\boldsymbol{b})$	=	vector of basis polynomials on simplex t_j
$B^d_\kappa(\boldsymbol{b})$	=	single basis polynomial of degree d
$\bar{b}$	=	aircraft span, m; wingspan, m
b_i	=	single barycentric coordinate component
$b_{t_j}(\boldsymbol{x})$	=	barycentric transform on simplex t_j
$b(\boldsymbol{x})$	=	barycentric transform of x
C_*	=	force/moment coefficient
$\boldsymbol{c}$	=	global B-coefficient vector
$\bar{c}$	=	average chord length, m
$\hat{\boldsymbol{c}}$	=	global B-coefficient estimator
$\boldsymbol{c}_{t_j}$	=	B-coefficient vector on simplex t_j
c_κ	=	single B coefficient
$c_\kappa^{t_j}$	=	single B coefficient on simplex t_j
d	=	polynomial degree
$\hat{d}$	=	number of basis functions per simplex
G	=	global B-coefficient matrix
H	=	global smoothness matrix
H_0	=	stall buffet model gain parameter
I_*	=	angular moment of inertia around $*$ axis, kg $\cdot$ m^2
J	=	cost function value
$\mathcal{J}$	=	cost function
$\mathcal{L}$	=	Lagrangian
M	=	Mach number
m	=	mass, kg
N	=	amount of time samples
n	=	amount of terms in a model structure; number of dimensions
p	=	roll rate, rad/s
$\boldsymbol{p}$	=	orthogonalized regression variable vector
Q_0	=	stall buffet model quality factor
q	=	pitch rate, rad/s
R^2	=	coefficient of determination
r	=	continuity order; yaw rate, rad/s
S	=	wing surface area, m^2
$\mathcal{S}^r_d$	=	degree d spline space with C^r continuity
T	=	total number of simplices
$\mathcal{T}$	=	triangulation
t_j	=	simplex with index j
U	=	Theil statistic
V_{TAS}	=	true airspeed, m/s
X	=	flow separation point variable; global regression matrix
$\tilde{X}$	=	substituted regression matrix
X_{thres}	=	stall buffet model threshold
x	=	regression variables
x_E, y_E, z_E	=	Cartesian position in F_E, m
$\dot{x}_E, \dot{y}_E, \dot{z}_E$	=	velocity components in F_E, m/s
$\boldsymbol{y}$	=	measurement vector; observation vector
$\hat{\boldsymbol{y}}$	=	model output vector
α	=	angle of attack, rad
α^*	=	X parameter for stall angle of attack, rad
β	=	angle of sideslip, rad
$\gamma_{k,j}$	=	Gram–Schmidt scaling parameter
δ_a	=	aileron deflection, rad
δ_e	=	elevator deflection, rad
δ_r	=	rudder deflection, rad
$\boldsymbol{\epsilon}$	=	vector of remnant
θ	=	pitch angle, rad; parameter vector
$\hat{\theta}$	=	optimal estimate of parameter vector
κ	=	multi-index
ρ	=	correlation
σ	=	standard deviation
τ_1	=	X parameter for lag, s
τ_2	=	X parameter for hysteresis, s
ϕ	=	roll angle, rad; orthogonal parameter vector
$\hat{\phi}$	=	optimal estimate of orthogonal parameter vector
ψ	=	heading angle, rad
ω_0	=	stall buffet model natural frequency, rad/s
$\nabla_{\boldsymbol{\delta}}\boldsymbol{\Phi}$	=	control effectiveness Jacobian

Subscripts

D	=	drag
L	=	lift
l	=	roll moment
m	=	pitch moment
n	=	yaw moment
p	=	partition index
T	=	thrust force
t_j	=	simplex identifier

Part of this work was presented as Paper 2018-1116 at the 2018 AIAA Guidance, Navigation, and Control Conference, Paper 2019-1320 at the AIAA SciTech 2019 Forum, and Paper 2021-1725 at the AIAA SciTech 2021 Forum; received 10 November 2022; revision received 3 March 2023; accepted for publication 18 April 2023; published online 24 August 2023.

*Associate Professor, Control & Simulation Section, Faculty of Aerospace Engineering, P.O. Box 5058; c.c.devisser@tudelft.nl. Member AIAA.

†Assistant Professor, Control & Simulation Section, Faculty of Aerospace Engineering, P.O. Box 5058; d.m.pool@tudelft.nl. Associate Fellow AIAA.

Y = lateral force
γ = multi-index
κ = multi-index

I. Introduction

MODELS of aircraft dynamics and aerodynamics play an increasingly important role in the aircraft design process, flight control system design, and piloted training simulators. For example, in 2019, flight simulator-based stall prevention and recovery training has become mandatory [1–3], for which aircraft stall models are needed to supply effective pilot training [4–6]. We are witness to the rise of drones, which are often characterized by highly nonlinear and unsteady aerodynamics (e.g., multirotors [7,8] and flapping wing drones [9,10]), which can only be fully understood and accounted for through modeling. Revolutionary new aircraft designs, both for civil aviation, to radically reduce emissions [11], as well as for Urban Air Mobility (UAM) applications [12,13], often ask for accurate models in early design stages and for control system design and operation. Because of the fact that especially critical damping and nonlinear aerodynamic characteristics can currently not be accurately derived from computational fluid dynamics predictions and (scaled) wind-tunnel experiments to obtain accurate and relevant models, there is still a strong focus on aerodynamic model identification based on collected flight-test data. This is particularly true for nonlinear regions of the flight domain, such as the high angle of attack, aerodynamic stall, and transonic flight regions. These developments thus require continuing innovations in aerodynamic model identification and flight-test procedures that go well beyond the accepted state of the art.

The section of Control & Simulation (C&S) of the Faculty of Aerospace Engineering at Delft University of Technology has a long history in the field of aircraft state reconstruction and system identification [14–20]. For example, a signature development has been the so-called two-step method, in which the combined state and parameter estimation problem is split into a state-estimation problem and an equation error-based parameter estimation problem [14]. Currently, the C&S group is still highly active on the topics of flight testing and model identification and is uniquely positioned due to direct access to a self-owned laboratory aircraft (Cessna Citation II, PH-LAB), six-degree-of-freedom (DOF) flight simulator [SIMONA Research Simulator (SRS) [21]]. More recently, the C&S group is applying its expertise and test facilities (Cyberzoo, Open Jet Wind Tunnel Facility) to the identification of aerodynamic models of flapping wing micro aerial vehicles [10,22–26] and multirotor drones [7,8], which bring with it unique challenges and opportunities, such as low-grade onboard sensors [27,28], highly nonlinear aerodynamics [8], and extreme power-to-weight ratios.

The goal of this paper was to provide an overview of current research on flight testing and model identification together with applications of the identified model at Delft University of Technology's C&S research group. To limit the scope and enable including a useful level of detail, recent work on aerodynamic model identification of drones is excluded from this paper. In the popular Delft University of Technology Master of Science-level course AE4320 "System Identification of Aerospace Vehicles," the main message is that in model identification a direct synergy is needed between 1) identification and modeling methods, 2) experiments performed to collect data for model identification, and 3) obtained results and desired applications of identified models, together forming the "system identification cycle." This paper is structured along the same lines and will present key developments in each of these three elements; see Fig. 1. For methods, we will present novel approaches to identify nonlinear stall dynamics models directly from stall flight-test data [29] and novel approaches to aerodynamic modeling based on multivariate splines [30]. For experiments, we will share our recent experiences with both standard quasi-steady identification flight tests and dedicated stall flight tests [29,31]. Finally, key recent

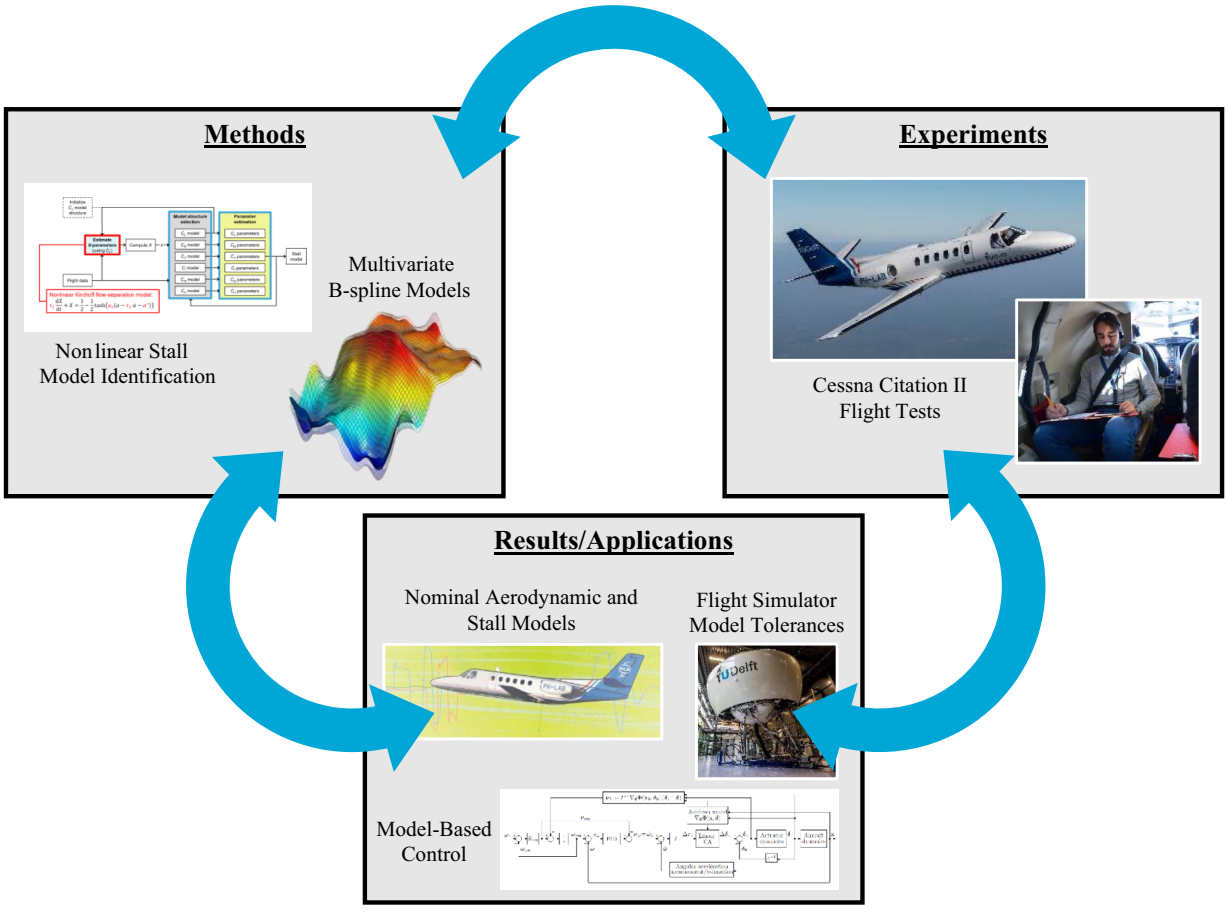

Fig. 1 Schematic overview of paper structure.

results from these methods and experiments will be summarized, as well as critical considerations for applications of identified aircraft models for model-based control [32,33] and pilot training in flight simulators [34,35].

This paper's structure is also aligned with Fig. 1. First, Sec. II describes new identification methods for application to flight-test data. Section III describes recent and innovative flight-test experiments performed to collect data for model identification of fixed-wing aircraft and drones. Section IV presents an overview of the key new results obtained and previously presented in [29,36], as well as selected crucial applications of identified models. The paper ends with final conclusions and an outlook for essential future research.

II. Methods

A. Nonlinear Stall Model Identification

1. Flow Separation Models

One of the most well-known model structures that has been proposed to model the nonlinear, dynamic, and time-dependent phenomena caused by aerodynamic stall is generally referred to as Kirchhoff's theory of flow separation [37]. This theory states that the relation between airfoil lift and the flow separation point X, which represents the fraction of the chord length affected by flow separation, can be included explicitly in traditional polynomial models for the aerodynamic forces and moments [see Eq. (1)] to account for changes in aircraft dynamics during stalled flight. The flow separation state X explicitly models the distance along the wing chord, where the flow separates, and ranges from 1 (for which flow is fully attached) to 0 (for which flow is fully separated). The flow separation state X is closely related to the aircraft's angle of attack α, and its dynamics can be modeled by the well-known first-order ordinary differential equation of Eq. (2):

$$C_L = C_{L_\alpha}\left(\frac{1+\sqrt{X}}{2}\right)^2 \alpha \tag{1}$$

$$\tau_1 \frac{\mathrm{d}X}{\mathrm{d}t} + X = \frac{1}{2}(1 - \tanh[a_1(\alpha - \tau_2\dot{\alpha} - \alpha^*)]) \tag{2}$$

The flow separation model of Eq. (2) contains four parameters that each characterizes a physical attribute of the stall. For example, τ_1 accounts for inertia in flow separation and reattachment, and thus adds lag to the dynamics of X compared to α variations. The second time constant, τ_2, models hysteresis effects on X. The shaping parameter a_1 sets the static mapping between X and α, and thereby accounts for the "abruptness" of the stall. Finally, α^* defines the angle of attack at which stall occurs. With Eq. (2), solving for an aerodynamic model's parameters (including the four flow separation parameters) becomes a nonlinear optimization problem, which makes it sensitive to initial conditions and computationally more demanding to solve. Still, previous research consistently shows the validity of this modeling approach [29,31,38,39].

An important focus of our current research focuses on the effectiveness of extending stall models with multiple flow separation state variables, as first proposed in [40]. This is an essential part of most stall models, as in reality it often happens that one wing stalls before the other, resulting in strong roll motions [3,5]. For example, in [41], we investigate the modeling improvement obtained by separately accounting for the flow separation on the left (X_L) and right (X_R) wings; see Eq. (3). This novel modeling approach provides a more versatile and physically meaningful method of modeling aircraft dynamics during stalls, but it also facilitates the explicit introduction of asymmetric model terms that are a direct function of their respective wing's flow separation state. In our view, such multistate flow separation models open the door to possible new ways of improving aerodynamic stall models identified from flight-test data [41]:

$$C_L = C_{L_0} + C_{L_{\alpha_L}}\left[\left(\frac{1+\sqrt{X_L}}{2}\right)^2 \alpha_L + \left(\frac{1+\sqrt{X_R}}{2}\right)^2 \alpha_R\right] \tag{3}$$

2. Stall Buffet Models

A key characteristic of a stall is the *stall buffet*, as buffeting is a crucial initial cue for pilots that indicates entering a potentially unsafe flight regime. The stall buffet, which occurs at high angles of attack, is the aerodynamic excitation due to flow separation causing pressure fluctuations over the wing [42–44]. In recent research, we have focused on improving the way in which the temporal variations in stall buffet intensity are implemented in stall models, by coupling buffet intensity directly to the models' flow separation state X [31] (see Sec. II.A.1) or the angle of attack α [44].

The stall buffet model proposed in [31] (see Fig. 2) was identified from buffet vibrations measured during flight tests with Delft University of Technology's Cessna Citation II laboratory aircraft. The basic characteristic feel of the buffet (i.e., the average frequency spectrum of the buffet vibrations) is modeled by passing unity-variance white noise through a second-order shaping filter; see Fig. 2. For modeling the Cessna Citation II's vertical stall buffet vibrations, the gain H_0, resonance frequency ω_0, and quality factor Q_0 of the second-order filter are used to create a band-pass filter focused on 12 Hz (75 rad/s) [31]. To match the buffet intensity variations that occur during approach to stall, stall, and stall recovery, the proposed buffet model of [31] uses an additional scaling with $1 - X$ (see Fig. 2) and is thus directly linked to the nonlinear stall dynamics model of Eq. (2). Finally, the stall buffet model contains a threshold on X (i.e., X_{thres}) to trigger the buffet model; only when $X < X_{\text{thres}}$ (for our Cessna Citation II data equal to 0.89 [31]) is the stall buffet model activated and adds vibrations to the aircraft's simulated vertical acceleration. This novel stall buffet model has been implemented for recent simulator experiments [34,35] and found to provide realistic buffet intensity variations.

3. Model Structure Selection

Also due to our reliance on stall flight-test data that contain only relatively mild quasi-steady and accelerated stall maneuvers, an essential factor is selecting a matching aerodynamic model structure that contains only those model terms needed to explain the data. For this, an explicit model structure selection algorithm based on the multivariate orthogonal function (MOF) modeling method described by Morelli et al. [45] and Grauer and Morelli [46] was developed [29]. The MOF enables objective and (semi-)automated model structure selection by orthogonalizing all candidate model terms, due to which terms can be added and evaluated independently of each other. In this way, an MOF algorithm iteratively "builds up" model structures from scratch based on a predefined pool of orthogonalized candidate regressor terms. Typically, this process is governed by a cost function that penalizes both modeling errors and model complexity [45]. As is typically done, for stall model identification, we use common aerodynamic model regressors, such as α, δ_e, and p. To facilitate direct identification of stall-related terms, the candidate pool is extended with the flow separation state X, as well as several mathematical transformations of X, as regressors (e.g. [29]):

$$\mathbf{1}, \alpha, \dot{\alpha}, \beta, \dot{\beta}, p, q, r, \delta_a, \delta_e, \delta_r, C_T, M,$$
$$X, (1-X), \left(\frac{1+\sqrt{X}}{2}\right)^2, \ \max(0.5, X) \tag{4}$$

The variables in Eq. (4) are referred to as the "base regressors," as they are considered as candidates directly, but also all unique

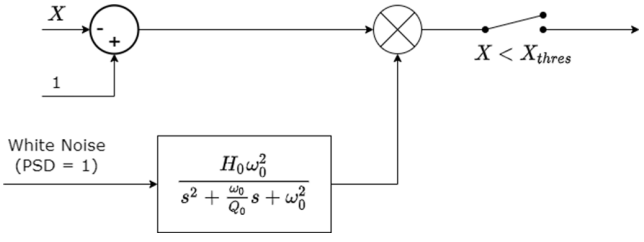

Fig. 2 Schematic overview of the stall buffet model proposed in [31], where PSD stands for Power Spectral Density.

product-wise combinations of these base regressors, up to and including a user-defined maximum order of n. As shown in Eq. (4), four base regressors that contain X are included. The regressor X itself can be used for explaining an effect that reduces or disappears during stall. The second regressor, $(1 - X)$, does the opposite; it only takes effect during flow separation. The third term is part of the term appearing in Kirchhoff's classical theory of flow separation, which would be created by taking the product of this term with α. Finally, the term $\max(0.5, X)$ was used to take into account some effects that change during stall but do not completely disappear for fully separated flow. Of course, a direct measurement of X is not available, but as explained in Sec. II.A.4 this can be solved after the flow separation model of Eq. (2) is estimated; then, X can be fully reconstructed.

The implemented model structure selection algorithm for stall model identification is shown in Fig. 3. The full details of this implementation can be found in [29]. The MOF algorithm is ran on each flight-test dataset separately (see Fig. 3) and also for first-order candidate regressor terms and second-order combinations of the candidate regressors of Eq. (4) (gray boxes). For selecting terms, an objective criterion that combines a fit error term [mean square error (MSE)] and a penalty term for model complexity (proportional to the model dimension n) is used [29]. The results of each iteration are then interpreted manually across all different identification datasets to decide which model terms are to be added to the model; see the "Interpret results" block in Fig. 3. To maintain an objective procedure as much as possible, regressors are added to the model when selected in at least 50% of the individual datasets. In cases where different, yet to some extent interchangeable, terms are selected across the (limited) training dataset, the relative usefulness of terms is judged based on the improved fit quality (MSE and R^2) on the validation datasets. Any selected terms are "frozen" into the model structure and are always included during later iterations. Iterations are run until no more new contributing model terms are found.

Ideally, the model structure selection algorithm converges to the same model structure for all datasets. It was found that this, however, was not the case for our flight-test data [29], especially when setting n larger than 2; this often causes functionally similar terms (e.g., α and $\alpha \cdot \delta_e$ for constant or slightly varying elevator deflections) to be included in the selected model structure. Thus, also including $n > 2$ terms may quickly conflict with the goal of selecting a parsimonious and consistent model structure.

4. *Model Identification and Parameter Estimation*

Incorporating the model structure selection approach outlined in Sec. II.A.3, we have proposed to split the model identification and parameter estimation for nonlinear stall models based on flight-test data in three steps [29], as outlined in Fig. 4.

First, in step 1, the flow separation model (X) parameters are estimated using nonlinear methods. The X parameters are identified using the measured C_L data, as the lift coefficient's dependency on the flow separation state is best documented in literature [37–39,47]. An initial assumption on the model structure of C_L needs to be made [e.g., Eq. (1)]. The implicit assumption is made that the dependence of the X parameters on the model structure is mild. When the model structure selection step of step 2 results in a different C_L model structure, the X parameters will also be estimated; see Fig. 4.

With step 1 completed, the estimated X parameters imply that also the model's X time response is known. This means that X, and other transformations of X [see Eq. (1)], can be used directly as potential (linear) regressors during model structure selection (step 2; see Sec. II.A.3) and parameter estimation (step 3), in parallel with measured flight states (e.g., α). Especially for the model structure selection in step 2, the fact that conventional linear least-squares methods can be used to fit models of the form of Eq. (1) enables quick iterations between selecting a model structure, directly solving for its parameters with least squares and validating the resulting model. As shown in Fig. 4, steps 2 and 3 are performed identically and independently for all aerodynamic force and moment equations. This three-step model identification and parameter estimation method was found to effectively deal with the inherently nonlinear aerodynamic

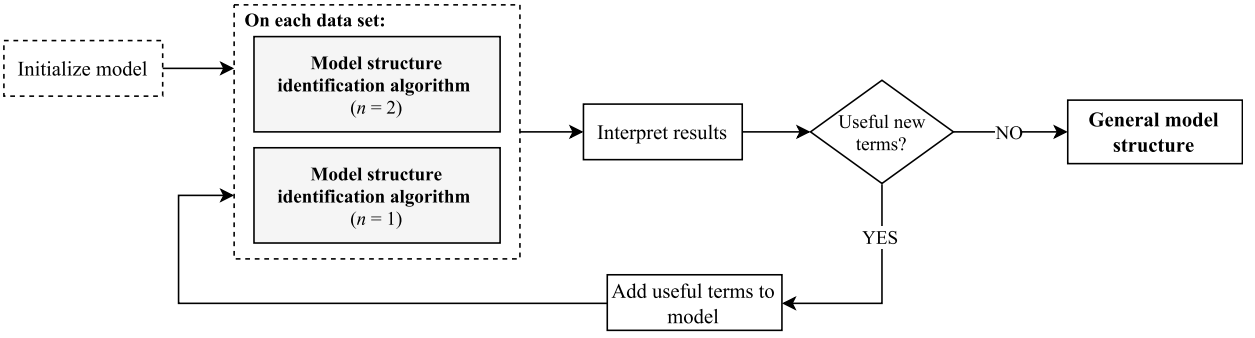

Fig. 3 Flowchart of the stall model structure selection algorithm [29].

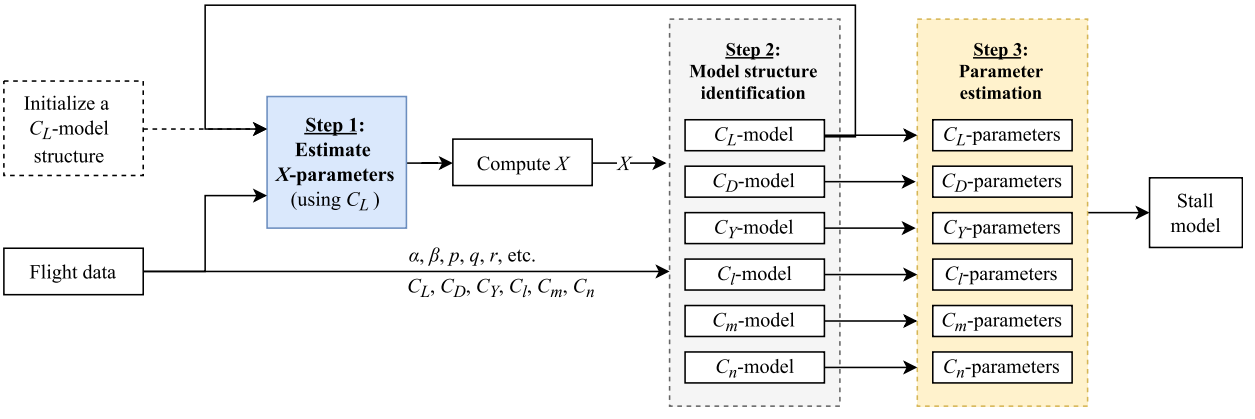

Fig. 4 Flowchart of the three-step nonlinear stall model identification approach [29].

model structure of nonlinear stall models and retrieve accurate and parsimonious models from measured stall flight-test datasets [29]; see Sec. IV.B.

B. Multivariate Splines for Aerodynamic Model Identification

Multivariate splines provide a powerful alternative to standard polynomial and lookup table-based modeling approaches; they combine the analytical, continuous nature of polynomials with the global nonlinear modeling capabilities of lookup tables. While one-dimensional (i.e., univariate) spline theory is well known and developed, multidimensional (i.e., multivariate) spline theory is still an active research field. At Delft University of Technology, a general multivariate "simplex" B-spline methodology was developed specifically for aerodynamic model identification [30,32,36,48–50]. Other authors have also introduced splines or equivalent polynomial smoothing (or "stitching") approaches for aerodynamic model identification, in particular the "model stitching" approach from [51,52] and the physically interpretable splines from [45]. Our methodology sets itself apart from these approaches by building on multivariate B-spline theory [53,54], resulting in a formally defined, general function approximator that allows the user to define splines in any number of dimensions, polynomial degrees, and continuity orders. At the same time, the linear regression method for multivariate B-splines from [36] is fully compatible with (online, distributed) parameter estimation schemes and model validation methods widely used in the aircraft system identification community.

This section presents an overview of the basic theory and necessary literature references required to develop state-of-the-art multivariate spline-based aerodynamic model identification and validation routines.

1. *Principles of Multivariate Simplex B-Splines*

Multivariate simplex B-splines are a type of multivariate spline that consists of a smooth combination of polynomials defined on simplex (e.g., triangular) intervals; see Fig. 5.

By combining any number of simplices into a *triangulation* [see Fig. 6 for a two-dimensional (2-D) example], an arbitrarily high approximation power can be obtained ([54], pp. 276–307). A triangulation $\mathcal{T}$ is a special partitioning of a domain in $\mathbb{R}^n$ into a set of T nonoverlapping simplices:

$$\mathcal{T} := \bigcup_{i=1}^{T} t_i, \quad t_i \cap t_j \in \{\emptyset, \tilde{t}\}, \quad \forall t_i, t_j \in \mathcal{T} \tag{5}$$

with the edge-simplex $\tilde{t}$ a k simplex with $0 \le k \le n-1$. It should be noted here that the term "triangulation" is also used for dimensions $n > 2$, even though they consist of tetrahedrons, pentachorons, etc.

The polynomial spline pieces on each simplex consist of local Bernstein basis functions $B_\kappa^d(\boldsymbol{b})$ of total polynomial degree d defined

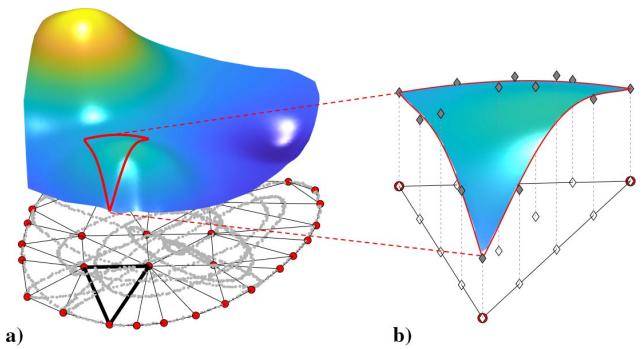

a) b)

Fig. 5 Principle of the multivariate simplex B-spline: a) a spline function with continuity defined on simplex intervals, and b) with each simplex supporting a locally defined basis polynomial scaled by B-coefficients (gray diamonds).

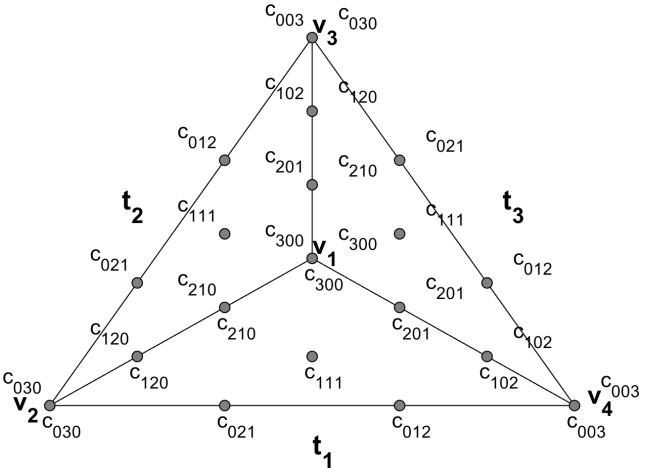

Fig. 6 B-net (B-coefficients indicated with c_{300} to c_{003}) for a third-degree 2-D spline function on three simplices (t_1 to t_3) defined by four vertices v_1 to v_4.

in terms of barycentric coordinates $\boldsymbol{b} = (b_0, b_1, \ldots, b_n)$, which are scaled by polynomial coefficients c_κ called *B coefficients*:

$$p(\boldsymbol{b}) = \sum_{|\kappa|=d} c_\kappa B_\kappa^d(\boldsymbol{b}) \tag{6}$$

This is the well-known B-form [53], with κ a multi-index defined as

$$\kappa = (\kappa_0, \kappa_1, \cdots, \kappa_n) \in \mathbb{N}^{n+1}, \quad \kappa_i \ge 0 \tag{7}$$

with $|\kappa| = \sum_0^n \kappa_i = d$, and $\kappa! = \prod_0^n \kappa_i!$. The B-form consists of a sum of $\hat{d} = (d+n)!/(n!d!)$ basis functions, which follows from the definition of κ. For example, for one-dimensional (1-D) Cartesian space ($n = 1$) and quadratic basis functions ($d = 2$) $\kappa \in (2,0)$, $(1,1)$, $(0,2)$, and hence, the corresponding B-form consists of a summation of three basis functions: $p(b_0, b_1) = c_{20}B_{20}^2(b_0, b_1) + c_{11}B_{11}^2(b_0, b_1) + c_{02}B_{02}^2(b_0, b_1)$.

The Bernstein basis functions in Eq. (6) are defined in barycentric coordinates as follows:

$$B_\kappa^d(\boldsymbol{b}) = B_\kappa^d(b_0, b_1, \ldots, b_n) = \frac{d!}{\kappa!} b_0^{\kappa_0} b_1^{\kappa_1} \cdots b_n^{\kappa_n} \tag{8}$$

With Eq. (8), we get for our earlier ($n = 1$, $d = 2$) example: $p(b_0, b_1) = c_{20}(2!/(2!0!))b_0^2 b_1^0 + c_{11}(2!/(1!1!))b_0^1 b_1^1 + c_{02}(2!/(0!2!))b_0^0 b_1^2$.

The barycentric coordinates $\boldsymbol{b} = (b_0, b_1, \ldots, b_n) \in \mathbb{R}^{n+1}$ of any Cartesian coordinate $\boldsymbol{x} = (x_1, x_2, \cdots, x_n) \in \mathbb{R}^n$ with respect to an n-simplext containing the vertices $(\boldsymbol{v}_0, \boldsymbol{v}_1, \ldots, \boldsymbol{v}_n)$ can be computed as follows:

$$\boldsymbol{x} = \sum_{i=0}^{n} b_i \boldsymbol{v}_i, \quad \sum_{i=0}^{n} b_i = 1 \tag{9}$$

The barycentric coordinate system is key to defining the stable local basis for the multivariate B-splines, which leads to numerically stable and sparse estimation and evaluation schemes, easy-to-implement continuity conditions, and bounded values for the B-coefficients of the spline pieces.

In [36], a useful vector formulation of the per-simplex B-form Eq. (6) was introduced:

$$p(\boldsymbol{b}) = \boldsymbol{B}_{t_j}^d(\boldsymbol{b}) \boldsymbol{c}_{t_j} \tag{10}$$

with $\boldsymbol{B}_{t_j}^d(\boldsymbol{b}) \in \mathbb{R}^{1\times\hat{d}}$ the vector of basis polynomials of degree d as in Eq. (8) and with $\boldsymbol{c}_{t_j} \in \mathbb{R}^{\hat{d}\times 1}$ the (column) vector of B-coefficients, both defined on the simplex t_j. The vector formulation requires an

explicit lexicographical sorting of the individual basis function terms and B-coefficients [55] as follows:

$$\boldsymbol{B}^d_{t_j}(\boldsymbol{b}) = \begin{bmatrix} B^d_{d,0,\ldots,0}(\boldsymbol{b}) & B^d_{d-1,1,\ldots,0}(\boldsymbol{b}) & \cdots & B^d_{0,\ldots,0,d}(\boldsymbol{b}) \end{bmatrix} \in \mathbb{R}^{1\times\hat{d}} \tag{11}$$

and the vector of B-coefficients on t_j is sorted correspondingly

$$\boldsymbol{c}_{t_j} = \begin{bmatrix} c_{d,0,\ldots,0} & c_{d-1,1,\ldots,0} & \cdots & c_{0,\ldots,0,d} \end{bmatrix}^\top = [c_\kappa]_{|\kappa=d|} \in \mathbb{R}^{\hat{d}\times 1} \tag{12}$$

The global vector of B-coefficients is obtained by collecting all T per-simplex B-coefficient vectors as follows:

$$\boldsymbol{c} = \begin{bmatrix} \boldsymbol{c}_{t_0} \\ \boldsymbol{c}_{t_1} \\ \vdots \\ \boldsymbol{c}_{t_T} \end{bmatrix} \in \mathbb{R}^{T\hat{d}\times 1} \tag{13}$$

The B-coefficients have a unique spatial ordering inside their supporting simplices called the B-net (see Fig. 6 for an example), which is essential for the definition of continuity between simplices [30,54,56,57], B-coefficient variance surfaces [36], distributed solvers [50,58], and local spline adaptation schemes [32]. The spatial location, in barycentric coordinates, of any B-coefficient of a dth-order B-form polynomial with respect to its parent simplex is computed using the multi-index κ from Eq. (7) as follows:

$$b_t(c_\kappa) = \frac{\kappa}{d} \tag{14}$$

Creating high-quality triangulations is not a trivial task, especially in dimensions higher than 2, where standard Delaunay triangulation methods result in ill-conditioned triangulations containing simplices with close to zero volume (so-called sliver simplices) [30]. For aircraft system identification, we obtain excellent results using an extension of Kuhn triangulation method [59,60]. Kuhn triangulation method, when applied on a unit hypercube, results in a symmetric triangulation that can be "stenciled" across the flight envelope, resulting in a triangulation consisting of well-conditioned simplices; see [30]. This algorithm works as follows: define $h = [0, 1]^n$ as the unit n-D cube, with $e^1, \ldots, e^n$ the set of unit vectors in $\boldsymbol{R}^n$. The set of $n!$ permutations of the sequence $1, \ldots, n$ is defined as S_n. Each of the elements $\pi \in S_n$ is used to construct a single n-simplex within the hypercube h. Hence, h can be divided into $n!$ simplices. Each simplex $t_\pi = \langle x^{(0)}_\pi, x^{(1)}_\pi, \ldots, x^{(n)}_\pi \rangle$ will now have vertices, which are recursively defined as follows:

$$x^{(j)}_\pi = x^{(j-1)}_\pi + e^{(\pi(j))}, \quad x^{(0)}_\pi = (0, 0, \ldots, 0), \quad 1 < j \le n \tag{15}$$

See Fig. 7 for an example of Kuhn triangulation of the three-dimensional (3-D) cube.

Note that while Kuhn triangulation is defined on hypercubes, resulting in rectangular global triangulations, it can be easily made nonrectangular. Simplices placed in nonphysical locations, or locations where no data are available, can be automatically removed from the triangulation if desired. If necessary, the resulting triangulation can also be locally refined by inserting vertices inside the Kuhn triangulation simplices or by moving vertices, as demonstrated in [30].

Formulating continuity of any order $m < d$ between the individual spline pieces is achieved by relating the B-coefficients of neighboring simplices with continuity conditions [57,61]. For example, the continuity condition to achieve continuity of order m between the simplices t_1 and t_2 in Fig. 6 is given by

$$c^{t_1}_{(\kappa_0,\ldots,\kappa_{n-1},m)} = \sum_{|\gamma|=m} c^{t_2}_{(\kappa_0,\ldots,\kappa_{n-1},0)+\gamma} B^m_\gamma(\sigma), \quad 0 \le m \le r \tag{16}$$

with $\gamma = (\gamma_0, \gamma_1, \ldots, \gamma_n)$ a multi-index independent of κ, and with σ the out-of-edge vertex of the simplex t_1 (i.e., the vertex $\boldsymbol{v}_3$ in $\boldsymbol{t}_1$, which is not on the edge between $\boldsymbol{t}_1$ and $\boldsymbol{t}_2$ in Fig. 6).

In [30], a more general formulation of the continuity conditions was introduced that is valid for general triangulations (e.g., continuity between $\boldsymbol{t}_1$ and $\boldsymbol{t}_3$, and $\boldsymbol{t}_2$ and $\boldsymbol{t}_3$ in Fig. 6). Eventually, to achieve C^m continuity over the entire spline function, all R continuity conditions for orders 0 to m for all neighboring simplex pairs are assembled into the so-called smoothness matrix $\boldsymbol{H}$ as follows:

$$\boldsymbol{H}\boldsymbol{c} = 0, \quad \boldsymbol{H} \in \mathbb{R}^{R\times T\hat{d}} \tag{17}$$

with $\boldsymbol{c}$ the global vector of B-coefficients from Eq. (13). Construction of the smoothness matrix is not trivial, especially if it is required to be of full rank. Refer to [30] for an in-depth discussion and examples.

2. *Linear Regression with Multivariate Splines*

The scattered data approximation problem for multivariate simplex B-splines can be formulated as the following sparse linear regression problem [36,62]:

$$\boldsymbol{Y} = \boldsymbol{X}\boldsymbol{c} + \boldsymbol{r} \in \mathbb{R}^N \tag{18}$$

with $\boldsymbol{Y}$ the vector containing all observations, with $\boldsymbol{c}$ the global vector of B-coefficients from Eq. (13), and with $\boldsymbol{r}$ a residual term. $\boldsymbol{X}$ in Eq. (18) is the sparse matrix of B-form regressors for all $i = 1, \ldots, N$ observations:

$$\boldsymbol{X} = \begin{bmatrix} \boldsymbol{B}^d_{t_0}(b(\boldsymbol{x}(i))) & \boldsymbol{B}^d_{t_1}(b(\boldsymbol{x}(i))) & \ldots & \boldsymbol{B}^d_{t_T}(b(\boldsymbol{x}(i))) \end{bmatrix}_{i=1}^N \in \mathbb{R}^{N\times T\hat{d}} \tag{19}$$

with $\boldsymbol{B}^d_{t_j}(b(\boldsymbol{x}(i)))$ as in Eq. (11) and with $b(\boldsymbol{x}(i))$ the barycentric coordinate of the data location (state) $\boldsymbol{x}(i)$ with respect to simplex t_j. It is important here to note that $\boldsymbol{x}(i) \notin t_j \rightarrow \boldsymbol{B}^d_{t_j}(b(\boldsymbol{x}(i))) = [0]$ by definition, that is, if a data point $\boldsymbol{x}(i)$ is located outside the simplex t_j, the corresponding columns in the regression matrix $\boldsymbol{X}$ are zero; this is the source of the sparseness of $\boldsymbol{X}$.

The general optimization problem for the B-coefficients can now be stated as follows:

$$\min_{\boldsymbol{c}} \mathcal{J}(\boldsymbol{c}), \quad \text{subject to } \boldsymbol{G}\boldsymbol{c} = \boldsymbol{g} \tag{20}$$

with $\mathcal{J}(\boldsymbol{c})$ a cost function in terms of the B-coefficients. The constraint matrix $\boldsymbol{G} \in \mathbb{R}^{G\times T\hat{d}}$ and constraint vector $\boldsymbol{g} \in \mathbb{R}^{G\times 1}$ in Eq. (20) are defined as follows:

$$\boldsymbol{G} = \begin{bmatrix} \boldsymbol{H} \\ \boldsymbol{W} \end{bmatrix}, \quad \boldsymbol{g} = \begin{bmatrix} \boldsymbol{0} \\ \boldsymbol{w} \end{bmatrix} \tag{21}$$

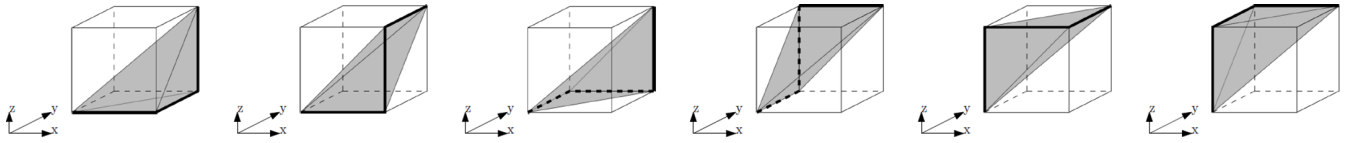

Fig. 7 Kuhn triangulation of the three-cube with six tetrahedrons.

with $\boldsymbol{H}$ the sparse smoothness matrix from Eq. (17), and with $\boldsymbol{W}$ and $\boldsymbol{w}$ any additional constraint matrix and vector, respectively. For example, $\boldsymbol{W}$ and $\boldsymbol{w}$ may hold hard constraints on individual B-coefficients, or may hold differential constraints [62] for the directional derivatives of the multivariate splines, which are useful when imposing Dirichlet, Robin, or Neumann boundary conditions when approximating partial differential equation solutions; see [63].

The effective degrees of freedom of the problem can be computed from the null space of the constraint matrix $\boldsymbol{G}$ from Eq. (21) :

$$N_c = \dim \ \ker \ \boldsymbol{G} \tag{22}$$

where N_c is in most cases significantly smaller than the total number of B-coefficients, in particular for higher continuity orders ($r > 1$) and lower degrees ($d < 5$) in higher-dimensional triangulations ($n > 3$).

3. B-Coefficient Estimators

A number of different linear estimators for the B-coefficients have been applied to the aircraft system identification problem. The simplest approach to spline model estimation method is the equality constrained generalized least-squares estimator for the B-coefficients, which was introduced in [36]. In this paper, a new formulation of this estimator is introduced, which includes Tikhonov [64] regularization to compensate for ill-defined per-simplex regression matrices resulting from data collinearities and/or insufficient data content:

$$\begin{bmatrix} \hat{\boldsymbol{c}} \\ \hat{\boldsymbol{\lambda}} \end{bmatrix} = \begin{bmatrix} \boldsymbol{Q} + \mu \boldsymbol{P} & \boldsymbol{G}^\top \\ \boldsymbol{G} & 0 \end{bmatrix}^+ \cdot \boldsymbol{X}^\top \boldsymbol{\Sigma}^{-1} \boldsymbol{Y} = \begin{bmatrix} \boldsymbol{C}_1 & \boldsymbol{C}_2 \\ \boldsymbol{C}_3 & \boldsymbol{C}_4 \end{bmatrix}^+ \cdot \boldsymbol{X}^\top \boldsymbol{\Sigma}^{-1} \boldsymbol{Y} \tag{23}$$

with $\hat{\boldsymbol{c}}$ the estimated B-coefficients, with $\hat{\boldsymbol{\lambda}}$ the estimated Lagrange multipliers, and with μ a tuning parameter that scales a square penalty matrix $\boldsymbol{P} \in \mathbb{R}^{T\hat{d} \times T\hat{d}}$. Note that if the problem is well conditioned, $\mu = 0$. In Eq. (23), $\boldsymbol{Q}$ is given by

$$\boldsymbol{Q} = \boldsymbol{X}^\top \boldsymbol{\Sigma}^{-1} \boldsymbol{X} \in \mathbb{R}^{T\hat{d} \times T\hat{d}} \tag{24}$$

with $\boldsymbol{\Sigma} = \mathrm{Cov}(\boldsymbol{r}) \in \mathbb{R}^{N \times N}$ the residual covariance matrix, which reduces to the identity matrix $\boldsymbol{I} \in \mathbb{R}^{N \times N}$ if the ordinary least-squares assumptions hold. Note that the Moore–Penrose pseudo-inverse in Eq. (23) is required because the smoothness matrix $\boldsymbol{H}$ will not be full rank if Eq. (16) is used to construct it without postconstruction filtering actions, resulting in a rank-deficient constraint matrix $\boldsymbol{G}$.

Using the top-left block $\boldsymbol{C}_1$ from Eq. (23), the generalized least-squares B-coefficient estimator can be simplified to

$$\hat{\boldsymbol{c}} = \boldsymbol{C}_1 \boldsymbol{X}^\top \boldsymbol{\Sigma}^{-1} \boldsymbol{Y} \tag{25}$$

In [61], Awanou et al., and in [65], Awanou and Lai introduced an efficient Lagrange multiplier-based matrix iterative solver (MIS):

$$\begin{aligned} \boldsymbol{c}^{(1)} &= \left(2\boldsymbol{Q} + \frac{1}{h}\boldsymbol{G}^T\boldsymbol{G}\right)^{-1}\left(2\boldsymbol{X}^\top\boldsymbol{\Sigma}^{-1}\boldsymbol{Y} + \frac{1}{h}\boldsymbol{G}^T\boldsymbol{g} - \boldsymbol{G}^T\boldsymbol{\lambda}^{(0)}\right) \\ \boldsymbol{c}^{(k+1)} &= \left(2\boldsymbol{Q} + \frac{1}{h}\boldsymbol{G}^T\boldsymbol{G}\right)^{-1}\left(2\boldsymbol{Q}\boldsymbol{c}^{(k)} + \frac{1}{h}\boldsymbol{G}^T\boldsymbol{g}\right), \quad k = 0, 1, 2, \ldots, M \end{aligned} \tag{26}$$

with $\boldsymbol{Q}$ as in Eq. (24), $\boldsymbol{G}$ as in Eq. (21), and with $\boldsymbol{\lambda}^{(0)}$ the initial guess for the Lagrange multipliers, which can be set equal to 0. The constant h in Eq. (26) is a small positive number. (For example, $h = 10^{-6}$ leads to adequate results in most cases.) Convergence is achieved when $|c^{(k+1)} - c^{(k)}| < \eta \cdot |\boldsymbol{X}^\top \boldsymbol{\Sigma}^{-1} \boldsymbol{Y}|$, with $\eta = 10^{-10}$ providing a good stopping condition in most cases. The iterative solver is highly efficient computationally when solving large problems, in which more than 100,000 B-coefficients are estimated, and converges quickly, in most cases within five iterations for low continuity orders (i.e., C^1 or less). In terms of computation time, a 100,000 B-coefficient problem with C^1 continuity is solved using a MATLAB sparse matrix solver (CHOLMOD) in 0.8 s, while a 200,000 B-coefficient problem with C^1 continuity is solved in 1.6 s, both on a single CPU core of an AMD Ryzen-9 5900X 12-core processor running at 3.7 GHz. This linear time scaling with the problem size highlights the high computational efficiency that can be obtained with sparse estimation problems resulting from local basis function approximations. To further improve performance, the authors of [62,66] present equality constrained recursive least-squares estimators for the B-coefficients, which only requires large-scale matrix inversion during initialization. These approaches are more suitable for online applications than Eq. (26). In [32], the method from [66] is used online in an adaptive control system for a simulated F-16 aircraft.

4. Distributed B-Coefficient Estimators

Modern parallel hardware architectures (e.g., graphics processing units) can be used to achieve significant speedup of large-scale problems, but only if the problem can be properly partitioned into smaller subproblems that can be executed in a parallel fashion. Multivariate simplex B-splines are particularly well suited for use with such distributed solvers because of their local basis property [58].

In [50], a variable splitting alternating direction method of multipliers (VSADMM) was proposed, resulting in a parallelizable distributed B-coefficient estimator for use in large-scale (online) aerodynamic model identification problems. The first step in creating a distributed B-coefficient estimator consists of partitioning the full triangulation into $P \leq T$ partitions:

$$\mathcal{T} = \bigcup_{i=1}^{P} \mathcal{T}_{p_i} \tag{27}$$

Creating the partitioning is not trivial, as many configurations are possible, including partitions consisting of a single simplex (i.e., $P = T$) or partitions with overlaps (see, e.g., [58,67] for details).

To define the VSADMM, a vector of coupling coefficients z_p is introduced for each partition p, such that $\boldsymbol{H}_p \boldsymbol{c}_p = \boldsymbol{z}_p$ [68,69]. The coupling coefficients are necessary when defining the distributed solver in Eq. (30). In this case, $\boldsymbol{H}_p$ is the set of columns of the global continuity matrix $\boldsymbol{H}$ that form continuity conditions with the per-partition set of B-coefficients $\boldsymbol{c}_p$ (i.e., $\boldsymbol{H} = [\boldsymbol{H}_1 \ldots \boldsymbol{H}_p \ldots \boldsymbol{H}_P]$ such that $\boldsymbol{H}_p \boldsymbol{c}_p = \boldsymbol{z}_p \to 0$). To satisfy the continuity conditions, the additional constraint $\sum_{p=1}^{P} \boldsymbol{z}_p = 0$ on the coupling coefficients is imposed. The VSADMM optimization problem can then be stated as follows:

$$\begin{aligned} &\mathrm{argmin}_{\boldsymbol{c}} \ \mathcal{J}(\boldsymbol{c}) = \sum_{p=1}^{P} \frac{1}{2} \|\boldsymbol{X}_p \boldsymbol{c}_p - \boldsymbol{Y}_p\|_2^2 \\ &\text{subject to } \boldsymbol{H}_p \boldsymbol{c}_p = \boldsymbol{z}_p \\ &\qquad \sum_{p=1}^{P} \boldsymbol{z}_p = 0 \end{aligned} \tag{28}$$

Setting up the augmented Lagrangian for this optimization problem, the constraints imposed on the sum of the coupling coefficients are exchanged for an indicator function $\mathcal{I}_{\mathcal{Z}}$, where $\mathcal{Z}$ is the convex set $\{[z_1, \ldots, z_P] : \sum_{p=1}^{P} z_p = 0\}$ [68]. This function evaluates to 0 when the solution is part of the set $\mathcal{Z}$, and ∞ otherwise, hence forcing the sum of the coupling coefficients to be exactly zero:

$$\begin{aligned} \mathcal{L}(\boldsymbol{c}, z, \lambda) = &\sum_{p=1}^{P} \frac{1}{2} \|\boldsymbol{X}_p \boldsymbol{c}_p - \boldsymbol{Y}_p\|_2^2 + \mathcal{I}_{\mathcal{Z}} + \lambda^T (\boldsymbol{H}_p \boldsymbol{c}_p - \boldsymbol{z}_p) \\ &+ \frac{\rho}{2} \|\boldsymbol{H}_p \boldsymbol{c}_p - \boldsymbol{z}_p\|_2^2 \end{aligned} \tag{29}$$

with λ the dual vector and with $\rho > 0$ a penalty factor chosen to penalize not satisfying the constraints, which improves convergence.

Exploiting the knowledge that the smoothness matrix $\boldsymbol{H}$ is sparse, it can be partitioned into a set of submatrices $\boldsymbol{H}_p$, which contain only continuity conditions within the partition p, and a set of submatrices $\boldsymbol{H}_{p,n}$, which describe interpartition continuity between the partition p and its direct neighbors n [58]. To construct these submatrices, let $\mathcal{H} = 1, 2, \ldots R$ be the row indices in the smoothness matrix $\boldsymbol{H}$. The subset $\mathcal{H}_p \in \mathcal{H}$ now contains the row indices of the internal constraints of partition p, while the subset $\mathcal{H}_{p,n}$ contains the row indices of the interpartition continuity conditions.

Information is shared between partitions using the coupling coefficients $\boldsymbol{z}_p$, because their overall sum should equal zero as in Eq. (28). Using the internal and interpartition sets, the update rule for the internal coupling coefficients $\boldsymbol{z}_p = 0$, and for the interpartition coupling coefficients $\boldsymbol{z}_{p,j}$ the update rule is given by [69]

$$\boldsymbol{z}_{p,j} = \left(\boldsymbol{H}_{p,j}\boldsymbol{c}_p + \frac{\lambda_{p,j}}{\rho}\right) - \frac{1}{m_j}\left(\sum_{i=1}^{P} \boldsymbol{H}_{i,j}\boldsymbol{c}_i + \frac{\lambda_{i,j}}{\rho}\right), \quad \forall j \in \left(\mathcal{H}_p \cup \mathcal{H}_{p,n}\right) \tag{30}$$

For the multivariate simplex B-splines, there are only two possibilities for m_j: either a constraint is internal (i.e., contained in $\mathcal{H}_p$) implying $m_j = 1$ or a constraint is interpartition (i.e., contained in $\mathcal{H}_{p,n}$) implying $m_j = 2$, because a continuity condition is always between two and only two simplices. Note that if $m_j = 1$, the coupling update will reduce to 0.

The complete VSADMM estimator is obtained by combining the coupling coefficient update [Eq. (31)], the B-coefficient update [Eq. (32)], and the dual update [Eq. (33)] as follows:

$$\boldsymbol{z}_{p,j}^{k+1} = \begin{cases} \left(\boldsymbol{H}_{p,j}\boldsymbol{c}_p^k + \dfrac{\lambda_{p,j}^k}{\rho}\right) - \dfrac{1}{2}\left(\displaystyle\sum_{i=1}^{P} \boldsymbol{H}_{i,j}c_i^k + \dfrac{\lambda_{i,j}^k}{\rho}\right), & \forall j \in \mathcal{H}_{p,n} \\ 0, & \forall j \in \mathcal{H}_p \end{cases} \tag{31}$$

$$\boldsymbol{c}_p^{k+1} = \left(\boldsymbol{X}_p^T\boldsymbol{X}_p + \rho\boldsymbol{H}_p^T\boldsymbol{H}_p\right)^{-1}\left(\boldsymbol{X}_p^T\boldsymbol{Y}_p + \rho\boldsymbol{H}_p^T\boldsymbol{z}_p^{k+1} - \boldsymbol{H}_p^T\lambda_p^k\right) \tag{32}$$

$$\lambda_p^{k+1} = \lambda_p^k + \rho\left(\boldsymbol{H}_p\boldsymbol{c}_p^{k+1} - \boldsymbol{z}_p^{k+1}\right) \tag{33}$$

Note that the B-coefficient and dual update iterations in Eqs. (32) and (33), respectively, do not depend on other partitions, and hence can run in parallel limited only by the number of parallel processors that are available; see Fig. 8. Only the coupling coefficient update [Eq. (31)] requires gathering of information from all partitions and subsequent broadcasting of the results to the parallel processes. Obtaining a stopping condition of the VSADMM is not trivial; see [50] for possible solutions.

5. *Multivariate B-Spline Model Validation*

Multivariate simplex B-spline models can be validated using the same analysis methods as those used with standard polynomial models, but because of the local basis property and spatial location of the B-coefficients they also allow for additional model quality assessment tools. The spline model residual ϵ is computed as follows:

$$\boldsymbol{\epsilon} = \boldsymbol{Y} - \boldsymbol{X}\hat{\boldsymbol{c}} \tag{34}$$

with $\boldsymbol{Y}$ the validation measurements, $\boldsymbol{X}$ the sparse matrix of B-form regressors for all $i = 1, \ldots, N$ validation data points, and with $\hat{\boldsymbol{c}}$ the global vector of estimated B-coefficients obtained with any estimator from Sec. II.B.3 or Sec. II.B.4. All standard residual-based global model quality metrics [e.g., residual rms, (adjusted) R^2, and variance accounted for] can be computed from Eq. (34). The user can also compute per-simplex residuals as follows:

$$\boldsymbol{\epsilon}_t = \boldsymbol{Y}_t - \boldsymbol{X}_t\hat{\boldsymbol{c}}_t, \quad t \in \mathcal{T} \tag{35}$$

Residual covariance matrix estimation is not a trivial task, and many different methods for constructing such matrices are presented in the literature (see, e.g., [70–72]). We use the method introduced by Klein and Morelli in [72] to calculate an $N_t \times N_t$ per-simplex residual covariance matrix $\boldsymbol{\Sigma}_t$:

$$\boldsymbol{\Sigma}_t = \frac{1}{N_t}\sum_{i=1}^{N_t-k} \epsilon_t(i)\epsilon_t(i+k), \quad k = 1, 2, \ldots, N_t \tag{36}$$

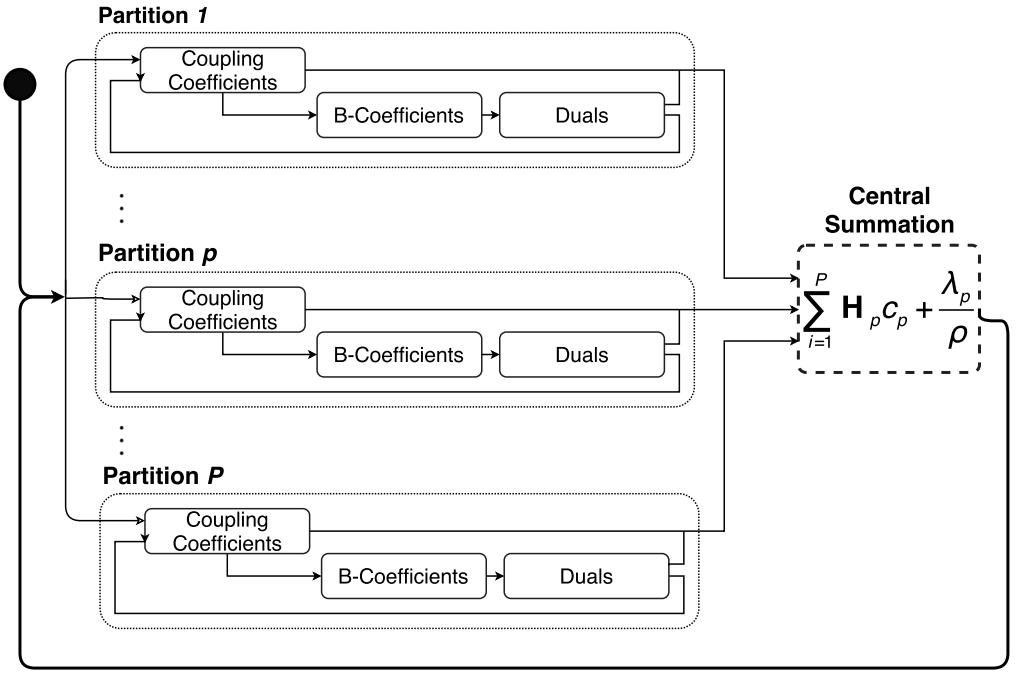

Fig. 8 Parallel flow of VSADMM.

The per-simplex residual covariance matrix blocks are then assembled into the global, block diagonal (sparse) $N \times N$ residual covariance matrix $\boldsymbol{\Sigma}_{\mathcal{T}}$. Here, it should be noted that Eq. (36) provides a lower bound for the covariances. The data contained within a simplex are not necessarily contiguous in time, and hence, some correlations in the residuals may be suppressed. In practice, however, trajectories tracked through phase-space result in per-simplex datasets that do contain at least segments of contiguous time data.

The B-coefficient covariance matrix provides a second key model quality metric, which follows directly from the generalized least-squares estimator [Eq. (25)]:

$$\mathrm{Cov}(\hat{\boldsymbol{c}}) = \boldsymbol{C}_1 \tag{37}$$

with parameter variances equal to the main diagonal of $\mathrm{Cov}(\hat{\boldsymbol{c}})$. Note that the iterative solver Eq. (26) also provides an approximation of the covariance matrix: $\mathrm{Cov}(\hat{\boldsymbol{c}}) \approx (2\boldsymbol{Q} + (1/h)\boldsymbol{G}^T\boldsymbol{G})^{-1}$. The spatial property of the B-coefficients from Eq. (14) leads to the B-coefficient variance surface or alternatively Cramér–Rao lower-bound surface [36], a unique property of the simplex B-splines. The variance surface allows the user to spatially pinpoint areas of high parameter variance in the model domain, which may indicate local data deficiencies, or a (local) model structure mismatch.

A final metric of multivariate spline model quality is its stability within the model domain. While this measure is hard, if not impossible, to determine for other nonlinear function approximators, such as neural networks, it is trivial when using simplex B-splines:

$$\min \boldsymbol{c}_{t_i} \leq p(\boldsymbol{b}) \leq \max \boldsymbol{c}_{t_i}, \quad \forall \boldsymbol{b} \in t_i \tag{38}$$

that is, the B-form polynomial $p(\boldsymbol{b})$ is bounded on the simplex t_i by the minimum and maximum B-coefficients $\boldsymbol{c}_{t_i}$ defined on that simplex. By extension, this implies that the global spline itself is bounded by $\min \boldsymbol{c}$ and $\max \boldsymbol{c}$.

6. *Procedure for Aerodynamic Model Identification with Multivariate Simplex B-Splines*

With all theory in place to identify and validate multivariate simplex B-spline models from scattered multidimensional data, a general procedure is presented for their use in aerodynamic model identification:

1) The dimension n is selected based on physical/expert knowledge of the system (i.e., which inputs and states are expected to play a role in the aerodynamic model).

2) The required continuity order r is determined; if the model is to be used for direct simulation (without linearization), C^0 continuity suffices. If the model is to be linearized at some point or used in a nonlinear model-based controller, C^1 is recommended. It should be noted that increasing the continuity order comes at the cost of reduced degrees of freedom to model the data according to Eq. (22) and often requires increasing the spline degree to maintain model quality.

3) If no triangulation exists, an initial (prototype) triangulation $\mathcal{T}$ is created in the form of a single Kuhn triangulated hypercube; see Sec. II.B.1. If the user is increasing the resolution of the triangulation, the stenciled Kuhn triangulated hypercube method can be used, and/or local triangulation refinements can be applied; see [30].

4) A data membership search is performed for all data points in the identification dataset; each data point is assigned to a single parent simplex. The user checks if each simplex $t \in \mathcal{T}$ contains at least $\hat{d} = (d+n)!/n!d!$ data points. If this is not the case, the resulting estimation problem may be ill-defined. This requires removal of the low-data volume simplex from the triangulation, application of additional (differential) constraints [62], or application of (per-simplex) Tikhonov regularization as in Eq. (23).

5) The spline degree d is selected. This is based on physical/expert insight into the system while taking into consideration the selected continuity order. The spline degree is equivalent to the degree of a standard Cartesian (physical) polynomial model fitting the data, that is, if a spline degree of $d = 3$ is selected, then it is expected that there are cubic physical polynomial terms present in the aerodynamic model. A new constraint matrix $\boldsymbol{G}$ must be formulated using Eq. (21).

6) A (distributed) estimator ($\hat{c}$) is formulated for the prototype spline model using, for example, Eq. (25); Eq. (26) for centralized approaches; or Eq. (32) for a distributed approach. The B-coefficients are estimated and B-coefficient (co)variance (surfaces) [Eq. (37)] analyzed. Model residuals are computed with Eq. (34) (global) or Eq. (35) (per-simplex) and analyzed using standard metrics {e.g., R^2, MSE, rms error (RMSE), and spline specific metrics such as the B-form bounds [Eq. (38)]}.

7) If the model does not meet validation accuracy requirements, the user first increases the spline degree and repeats steps 5 and 6. However, if this is not physically meaningful or does not sufficiently improve the model, the user must improve the triangulation and repeat steps 3–6.

When using multivariate splines for aerodynamic model identification, the user should be aware that the arbitrarily high approximation power of the multivariate splines can lead to local overfitting. Overfitting can easily be detected during spline construction using solution system condition numbers and pinpointed by analyzing the B-coefficient variances, which peak in areas where local overfitting is present. However, even though multivariate spline models can have a large number of parameters [e.g., >250,000 in the case of some five-dimensional (5-D) submodels of the highly nonlinear Innovative Control Effectors (ICE) aircraft [73]], these parameters are only locally "active." This is a direct result of the local basis property of the multivariate B-splines. In the case of ICE, the 5-D spline model contains 56 B-coefficients per simplex, implying that 56 B-coefficients need to be estimated per simplex (and evaluated at every time step). In addition, a significant subset of these 56 B-coefficients is used to obtain smoothness between neighboring simplices and is constrained by the continuity conditions. Hence, a more accurate metric of the multivariate simplex B-spline model complexity is the DOF of the model N_c, which is computed using Eq. (22). In the case of the aforementioned 5-D ICE submodel, enforcing C^1 continuity reduces the degrees of freedom from >250,000 to just 768, that is, 99.7% of all B-coefficients are required just to achieve C^1 continuity.

III. Flight-Test Experiments

A. Flight-Test Vehicle and Hardware

In support of our aerodynamic and stall model identification research, flight tests are performed in the Cessna Citation II laboratory aircraft (call sign PH-LAB) that is co-owned by Delft University of Technology's Faculty of Aerospace Engineering and The Netherlands Aerospace Center [Nationaal Lucht en Ruimtevaartlaboratorium (NLR)]. Schematic views of the aircraft can be found in Fig. 9. Tables 1 and 2 contain general mass [based on the aircraft's basic empty weight (BEW)] and geometric properties, and list the flight-test equipment relevant to this research. The aircraft is equipped with an advanced flight-test instrumentation system, which connects and centrally logs data from installed sensors (see Table 2), such as an external air data boom that is mounted on the nose of the aircraft for angle of attack and angle of sideslip measurements; see Fig. 9. Finally, a custom in-house-developed fly-by-wire system is available for this aircraft [74,75], which enables providing automated flight-test inputs.

B. Stall Flight-Test Maneuvers

For example, for our recent experiments on stall model identification [29,31], we have performed dedicated flight tests focusing on symmetric quasi-steady stall maneuvers and accelerated stall maneuvers with bank angles of 30–45 deg (approximately 1.1 or 1.3 g). To collect valuable data for model identification, we ensure that before each stall maneuver the aircraft trimmed in nominal flight, to include stall entry, the stall itself, as well as recovery phases. Figures 10a and 10b show an overview of all flight-test recordings collected in the experiment of van Ingen et al. [29], which shows a focus on stall data

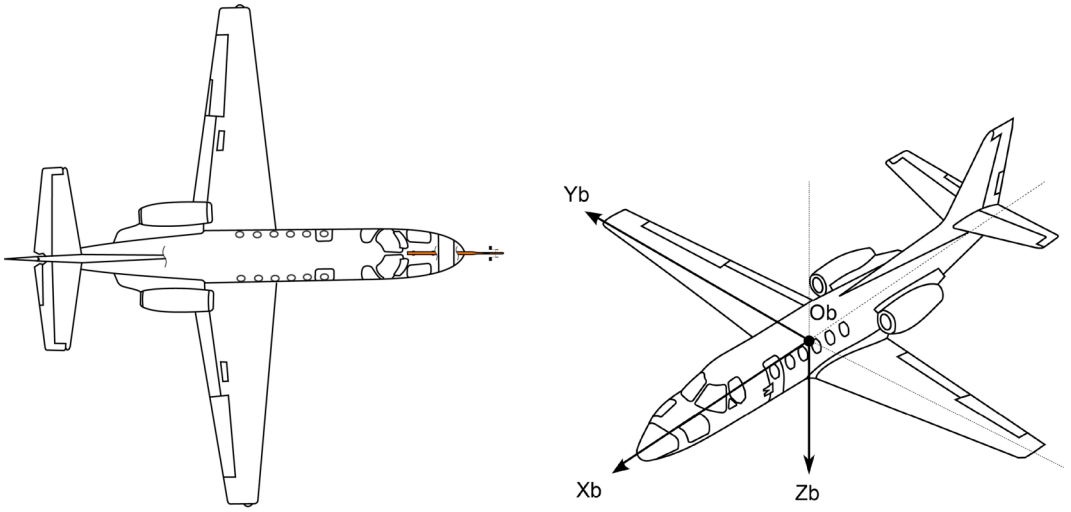

a) Top view b) 3D view

Fig. 9 Schematic views of the Delft University of Technology/NLR PH-LAB laboratory aircraft, including the body-fixed reference frame definition.

Table 1 PH-LAB dimensions and mass properties (BEW)

Parameter	Value
Dimensions	
S	30.0 m^2
$\bar{b}$	15.9 m
$\bar{c}$	2.09 m
Mass and inertia	
m	4,157 kg
I_{xx}	12,392 kg · m^2
I_{yy}	31,501 kg · m^2
I_{zz}	41,908 kg · m^2
I_{xz}	2,252.2 kg · m^2

collection at altitudes between 4500 and 5500 m, for which angles of attack up to 27 deg were achieved.

A focus area of our recent stall flight testing has been the refinement of flight-test inputs that are provided during the portion of stalled flight, to achieve sufficient excitation of the aircraft's dynamics to facilitate model identification, as well as collecting direct measurements of degraded control surface effectiveness. For example, as illustrated in Fig. 10c, we have used manually applied quasi-random flight-test inputs on multiple control surfaces, based on a technique described by Morelli et al. [45]. Figure 10c shows the change in angle of attack α, in gray for reference, to clearly indicate where the stall occurs. In blue, the aileron, elevator, and rudder input traces are shown; for the elevator, pilot inputs are required to keep the aircraft at the desired stalled flight condition, while (semi-) random inputs for excitation are visible on the aileron and rudder inputs. Alternatively, we have leveraged the PH-LAB's experimental fly-by-wire control system [74,75] to execute fully automated flight-test inputs to achieve more consistent and repeatable flight-test experiments; see Fig. 10d. Overall, the result of these focused flight-test inputs is that they directly increase the essential excitation in our flight-test datasets, which greatly benefits model identification accuracy [29].

C. Flight-Test Data Preprocessing

An integral part of all flight tests is that next to the aerodynamic data collected, the many sensor measurements will require preprocessing to make signals suitable for model identification. For stall flight tests, for example, a number of measured signals are affected by the stall buffets that occur during the (approach to) stall in most aircraft. The buffet vibrations are vital to a realistic stall model implementation in a simulator, but these are modeled by a separate buffet model [31,44]. As the buffets in general do not directly affect the aircraft's kinematic movement, it is essential that the strong impact the stall buffet may have on certain measurements is removed before flight path reconstruction or model identification. Figure 11 shows example air data boom measurement data from [29] for the angle of attack that shows how strongly the α measurement is affected by stall buffet vibrations. In red, Fig. 11 shows the same data but then preprocessed with a fourth-order Butterworth filter (applied both in forward and reverse directions to avoid filter-induced phase lag) to remove the buffet vibrations.

IV. Results and Applications

A. Nominal Envelope Aerodynamic Model Identification

1. *Multivariate Splines-Based Model of the Cessna Citation II*

The multivariate simplex B-splines introduced in Sec. II.B were used to identify a global aerodynamic model of the Cessna Citation II

Table 2 Flight-test equipment installed on the PH-LAB Cessna Citation II aircraft, including the measured variables relevant to this research

Name	Explanation	Measures	Variables	Units
GPS	Global positioning system	Position in F_E	x_E, y_E, z_E	m
		Velocity in F_E	$\dot{x}_E, \dot{y}_E, \dot{z}_E$	m/s
DADC	Digital air data computer	Total airspeed	V_{TAS}	m/s
AHRS	Attitude and heading reference system	Aircraft attitude	ϕ, θ, ψ	rad
		Body rotation rates	p, q, r	rad/s
		Body specific forces	A_x, A_y, A_z	m/s^2
Synchro	Angle measurements	Control surface deflection	$\delta_a, \delta_e, \delta_r$	rad
Boom	Air data boom	Air incidence angle	α, β	rad

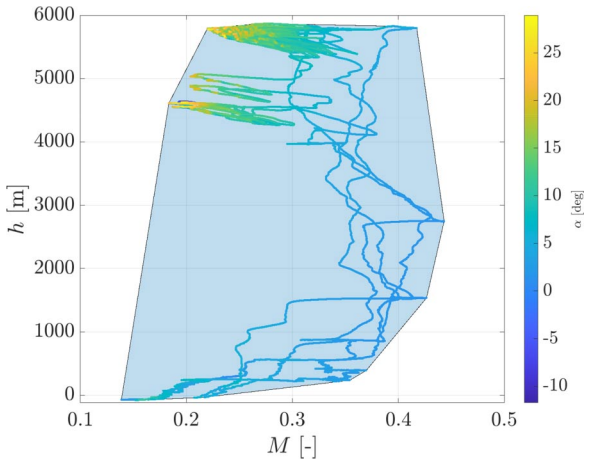

a) Flight envelope: (h, M)

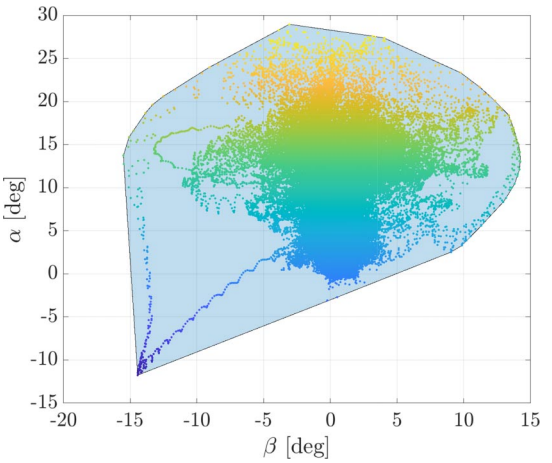

b) Flight envelope: (α, β)

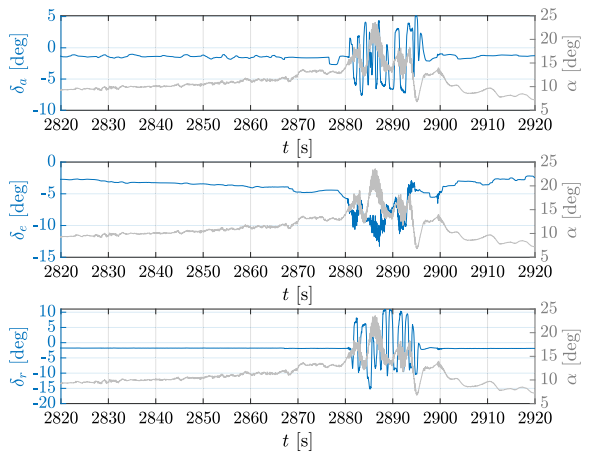

c) Flight test inputs: quasi-random

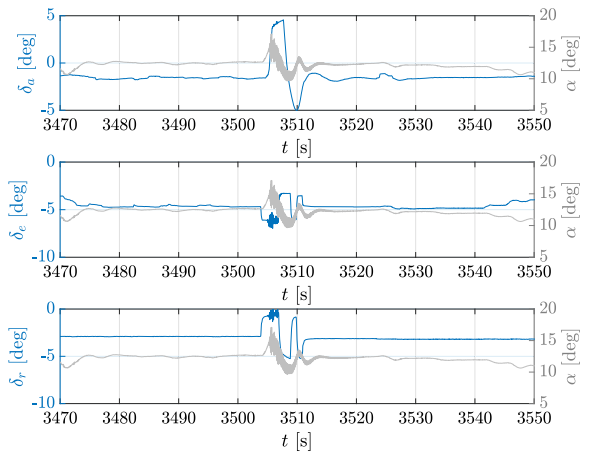

d) Flight test inputs: 3211

Fig. 10 Example of Cessna Citation II stall flight-test results from [29]: a–b) the part of the flight envelope covered in the flight tests; c–d) examples of (manual) quasi-random and (automated) 3211 flight-test inputs, respectively, that were given during stalled flight to obtain data on degraded control surface effectiveness.

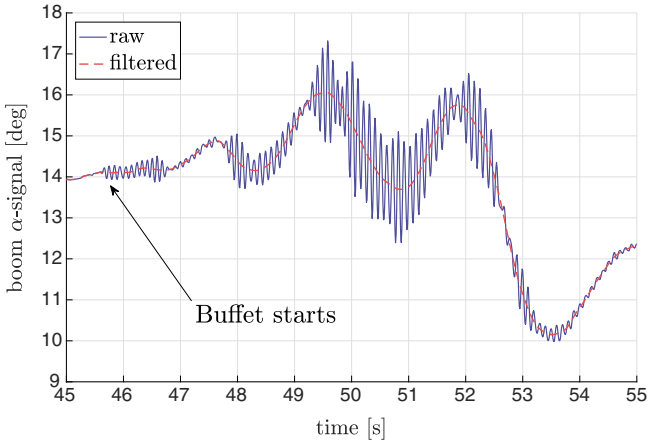

a) Boom α measurement time trace

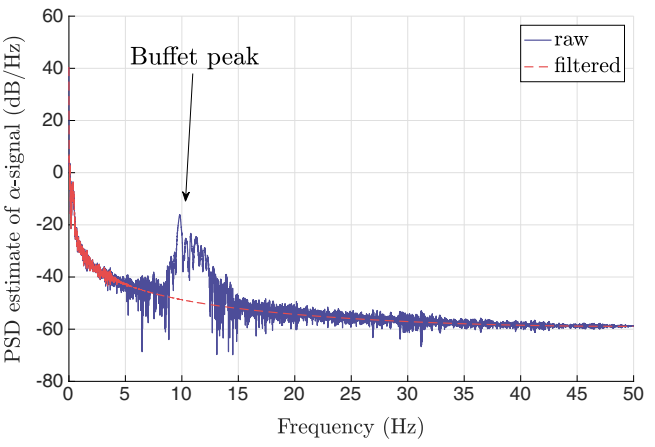

b) Boom α measurement spectrum

Fig. 11 Examples of raw and filtered angle-of-attack air data boom measurements from stall flight-test data [29], where PSD stands for Power Spectral Density.

laboratory aircraft (see Sec. III.A) from flight-test data. In total, 8 million data points resulting from 247 doublet and 3211 maneuvers (79 longitudinal, 62 lateral, and 106 coupled) were used to create the multivariate B-spline model.

An iterated extended Kalman filter was used for flight path reconstruction, the first step of the two-step method [20]. The model structure selection process for the multivariate simplex B-splines presented in Sec. II.B.6 was used to determine adequate model structures for all force and moment coefficient models.

Table 3 shows the results of the validation of the multivariate spline-based aerodynamic models using an independent subset of the flight data. The models for C_Z, C_l, and C_m and C_n are of high

Table 3 Results of the Citation II spline model validation

Coefficient	Spline model	Degree	Continuity	Simplices	B-coefficients	R^2	Error rms	Relative error rms, %
C_X	$f_X(\alpha, \delta_e, M)$	5	C^1	6	336	0.88	1.6e–2	4.68
C_Y	$f_Y(\beta, \delta_r, r)$	3	C^1	6	120	0.42	3.8e–2	7.18
C_Z	$f_Z(\alpha, \delta_e, q, M)$	6	C^3	21	4410	0.92	6.5e–2	3.40
C_l	$f_l(\beta, \delta_a, p)$	5	C^3	6	336	0.64	9.6e–4	1.57
C_m	$f_m(\alpha, \beta, \delta_e, q)$	5	C^2	21	2646	0.72	8.9e–3	2.69
C_n	$f_n(\beta, \delta_r, r, M)$	5	C^3	22	2772	0.66	1.9e–3	2.48

quality with relative rms scores of less than 5% (implying 95% global accuracy). The model for C_Y with a relative rms score of 7.2% has a lower quality, albeit with a global accuracy that is higher than 90%. This lower quality can be explained by a lack of excitation along the Y axis, resulting in a triangulation with most of the data close to the trim point (center of the triangulation) and very little data present at the edges of the triangulation, causing high variances in these regions, and consequently lower-quality model validation scores. The total number of B-coefficients per spline model is also shown, but as mentioned in Sec. II.B.6, the actual DOF of the models is significantly lower due to the continuity conditions that constrain an increasing number of B-coefficients as the continuity order increases.

2. *Multivariate Splines-Based Aerodynamic Model for the ICE Aircraft*

The Lockheed Martin ICE configuration is an overactuated 65 deg sweep, highly maneuverable, supersonic tailless flying wing with 13 ICE with nonnegligible nonlinear cross-effector couplings resulting in a non-control affine system [33,73,76,77]. The configuration of the ICE control effectors is shown in Fig. 12.

At Delft University of Technology, a new incremental nonlinear control allocation (INCA) method was introduced that exploits the nonlinear state–effector and effector–effector couplings [33]. The core element of INCA is a first-order continuous global multivariate simplex B-spline model of the force and moment coefficients of ICE with the following structure:

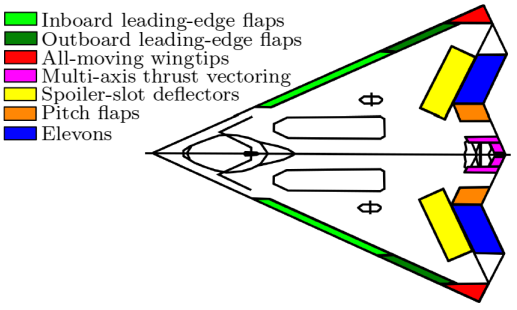

Fig. 12 Lockheed Martin ICE aircraft.

$$
\begin{aligned}
S_i = {} & S_{i_1}(\alpha, M) + S_{i_2}(\alpha, \beta, M) - S_{i_3}(\alpha, \beta, \delta_{\text{LIBLEF}}) \\
& - S_{i_4}(\alpha, \beta, \delta_{\text{LIBLEF}}, \delta_{\text{LOBLEF}}, M) + S_{i_5}(\alpha, \delta_{\text{LSSD}}, \delta_{\text{LEL}}, M) \\
& + S_{i_6}(\alpha, \delta_{\text{LSSD}}, \delta_{\text{RSSD}}, \delta_{\text{PF}}, M) + S_{i_7}(\alpha, \beta, \delta_{\text{LAMT}}) \\
& + S_{i_8}(\alpha, \delta_{\text{LEL}}, \delta_{\text{LAMT}}) + S_{i_9}(\alpha, \delta_{\text{LOBLEF}}, \delta_{\text{LAMT}}) \\
& - S_{i_{10}}(\alpha, \delta_{\text{REL}}, \delta_{\text{RAMT}}) - S_{i_{11}}(\alpha, \delta_{\text{ROBLEF}}, \delta_{\text{RAMT}}) \\
& + S_{i_{12}}(\alpha, \beta, \delta_{\text{LSSD}}) + S_{i_{13}}(\alpha, \beta, \delta_{\text{RIBLEF}}) \\
& + S_{i_{14}}(\alpha, \beta, \delta_{\text{RIBLEF}}, \delta_{\text{ROBLEF}}, M) - S_{i_{15}}(\alpha, \delta_{\text{RSSD}}, \delta_{\text{REL}}, M) \\
& - S_{i_{16}}(\alpha, \beta, \delta_{\text{RAMT}}) - S_{i_{17}}(\alpha, \beta, \delta_{\text{RSSD}}) + \frac{bp}{2V} S_{i_{18}}(\alpha, M) \\
& + \frac{br}{2V} S_{i_{19}}(\alpha, M) \qquad (39)
\end{aligned}
$$

with $i = \{l, m, n, X, Y, Z\}$, where each model term S_{i_n} is a multivariate B-spline function with C^1 continuity. This model was identified from the ICE aerodynamic database [73] using both a global approach from Sec. II.B.3 and the distributed approach from Sec. II.B.4; see [50]. The full spline-based aerodynamic model consists of 108 spline functions of dimensions varying from 1-D to 5-D. In Fig. 13, an illustration is given of the significant high-dimensional nonlinearities present in the ICE spline models.

In Fig. 14, the normalized (with respect to the minimum and maximum submodel outputs) RMSE on a validation dataset is plotted for all 108 multivariate B-spline submodels that together form the ICE spline-based aerodynamic model. The submodel indices (horizontal axis) correspond to those in Eq. (39). The largest normalized validation error is 1.4%. Each aerodynamic force and moment coefficient consists of 19 spline models with a total of 486e3 B-coefficients. As mentioned in Sec. II.B.6, the total DOF of the model is significantly less (≈5000); more than 99% of all B-coefficients are constrained by continuity conditions to achieve C^1 continuity between spline pieces.

In Fig. 15, the convergence of the distributed VSADMM approach is shown as a function of the total number of iterations. From this figure, it can be concluded that when using Kuhn triangulation, excellent convergence toward the global solution can be obtained,

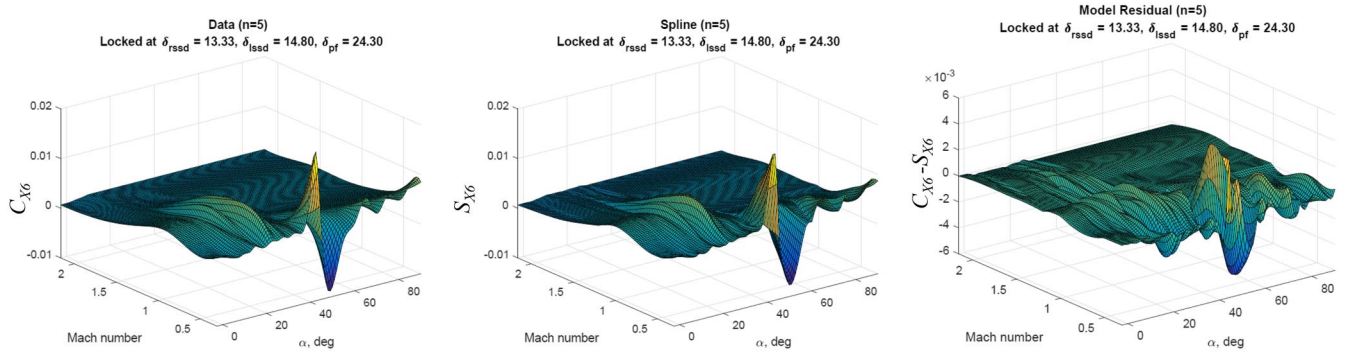

Fig. 13 Example of ICE spline-based aerodynamic model: slices through the original 5-D (cubic interpolated) dataset (left), the 5-D spline function S_{X_6} (middle), and the model residual (right).

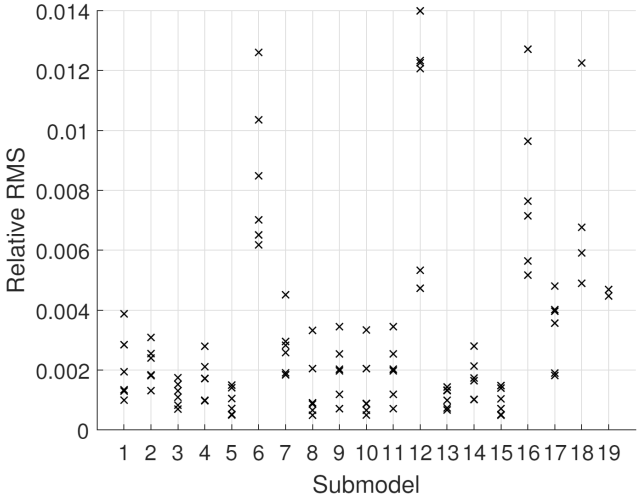

Fig. 14 ICE spline model validation results for all 108 submodels (submodel index on horizontal axis).

in particular when a per-hypercube [(3)-Hyp in the figure] partitioning system is used.

Finally, a multivariate simplex B-spline model obtained with the distributed VSADMM method is validated within an open-loop six-DOF time-based simulation framework against the output of the lookup table-based aerodynamic model from [73]. In its default configuration, the lookup table-based model uses mixed linear and cubic interpolation in each of its 108 (table-based) submodels. In Table 4, the aerodynamic force and moment coefficients predicted by the spline-based aerodynamic model are validated against those predicted by the lookup table-based model for a set of four 10 s simulation runs with specified control surfaces deflecting after 4 s.

In Fig. 16, a 10 s open-loop simulation run, with all control surfaces moved to their maximum deflection setting after 4 s, is shown for both the multivariate spline and lookup table-based models. Here, the multivariate spline model clearly can match the lookup table-based model for most coefficients. Only the C_l model shows significant mismatch; in this case, this is caused by the state moving out of bounds of the model domain after the aggressive (open-loop) input, highlighting to different clipping behavior between the spline and lookup table-based models.

Finally, the computational performance of the multivariate spline-based aerodynamic models during simulation was assessed. The complete (108 submodels) C^0 multivariate spline model from [33] is evaluated at a given state within on average 0.01 ms on a single

Table 4 Normalized RMSE between the original lookup table-based model of ICE from [74] and the multivariate B-spline model during 10 s simulation runs

Input	C_X, %	C_Y, %	C_Z, %	C_l, %	C_m, %	C_n, %
None	2.14	1.90	2.82	3.36	2.75	2.18
Elevons/all-moving wingtips	1.75	4.39	2.50	1.99	1.23	2.78
differential leading-edge flaps/spoiler–slot–deflectors	1.54	2.10	1.71	6.54	2.76	1.68
All	1.20	1.56	1.55	6.41	2.49	3.03

CPU core of an AMD Ryzen-9 5900X 12-core processor running at 3.7 GHz. The complete C^1 model presented in this paper can be evaluated on average in less than 0.10 ms on the same hardware at any given state. The lookup table-based model evaluates on average in 0.12 ms on the same hardware. Hence, increasing the continuity order of a multivariate spline-based aerodynamic model increases the computational cost of model execution, which is caused by the fact that a higher degree must be selected to achieve adequate modeling accuracy with the additional continuity constraints. However, the computational cost for a C^1 continuous model is at least comparable to the lookup table-based model.

B. Aircraft Stall Modeling

1. *Model Structure Selection*

The proposed model structure selection algorithm (see Sec. II.A.3) was found to be highly effective for selecting appropriate aerodynamic model terms. Figure 17 shows example results of the approach outlined in Fig. 3 for the model for the lift coefficient C_L. The x-axis range in Fig. 17 shows that 27 of the 34 available stall flight-test datasets were used in [29] as training data. Furthermore, the results of the first iteration of adding model terms are shown in Fig. 17a, while Fig. 17b shows the second iteration's results. Gray bars indicate terms that were already frozen into the model prior to both iterations.

For the first iteration, three terms were found to be useful (i.e., occurring in more than 50% of datasets; dashed line in Fig. 17): α; $((1+\sqrt{X})/2)^2$; and the combination of the two, the Kirchhoff term: $((1+\sqrt{X})/2)^2\alpha$. Based on the first iteration result, only the latter term was selected, as it resulted in the largest improvement in model validation fit quality. For the second iteration (see Fig. 17b), further angle-of-attack-related terms (e.g., α or α^2) were identified as effective additions. After further experimenting with several variations of α-related terms, in [29] the term $(\alpha - 6\ \text{deg})_+^2$ was in the end added to the C_L model. This notation indicates a univariate quadratic spline in α with C^1 continuity at $\alpha = 6$ deg, which only adds an additional effect of the angle of attack on C_L for $\alpha > 6$ deg:

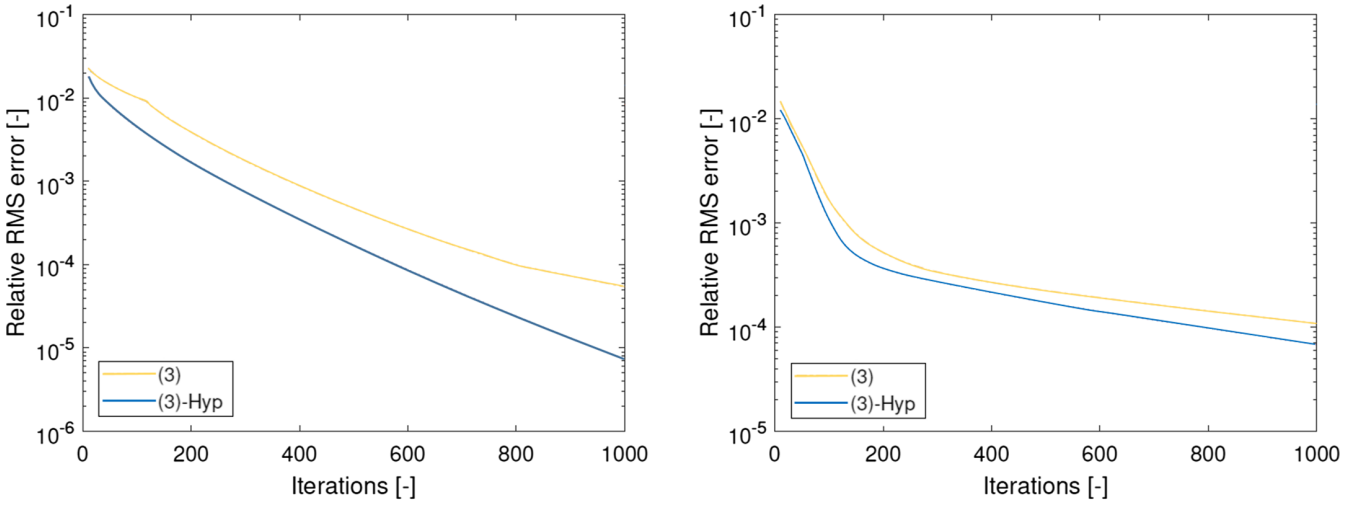

a) $\rho = 1.0$ **b) $\rho = 0.01$**

Fig. 15 Convergence of the distributed algorithm for different values of the penalty factor ρ at 0% noise intensity; (3) is a multihypercube per partition 3-D simplex B-spline; (3)-Hyp is a per-hypercube partitioned 3-D simplex B-spline (both using Kuhn triangulation).

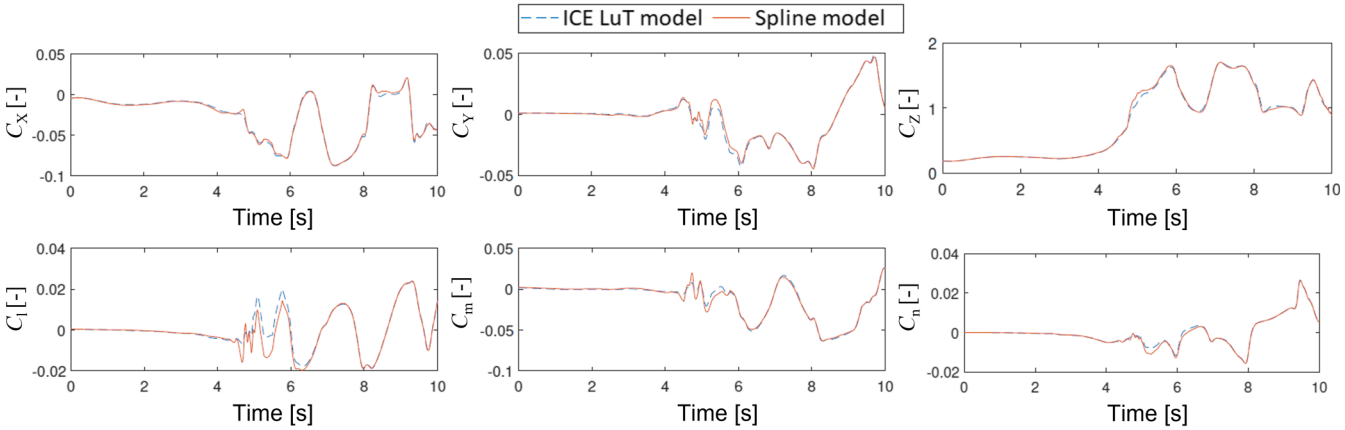

Fig. 16 Comparison of force and moment coefficients between lookup table (LuT) and spline-based aerodynamic model for a 10 s simulation run with all effectors at maximum deflection.

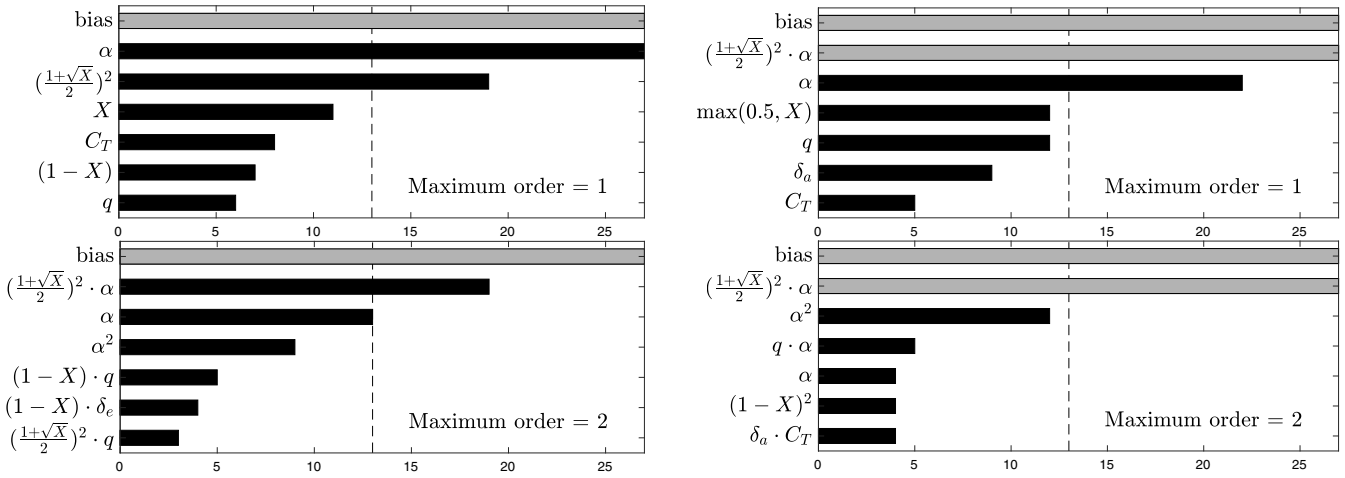

a) First iteration **b) Second iteration**

Fig. 17 Model structure selection outcomes for the C_L model; the vertical dashed line indicates the reference limit of 50% of the training datasets, while gray bars indicate a term frozen in the model prior to that iteration [29].

$$(\alpha - 6\ \text{deg})_+^2 = \begin{cases} (\alpha - 6\ \text{deg})^2 & \text{when } \alpha \geq 6\ \text{deg} \\ 0 & \text{when } \alpha < 6\ \text{deg} \end{cases} \tag{40}$$

During a third iteration, no new model terms were found. Overall, the fact that the final C_L model obtained from the proposed model structure selection contains the classical Kirchhoff equation as its dominant term, as would be expected based on flow separation theory and available literature [39], is further proof of the effectiveness of this approach. Similarly, in [29], the detailed results for the obtained model structures for all aerodynamic force and moment coefficients are presented. The final obtained model structures, which are seen to include explicit X-dependent regressors in the C_L, C_D, and C_m models, are listed in Eq. (41):

$$\hat{C}_L = C_{L_0} + C_{L_\alpha}\left(\frac{1+\sqrt{X}}{2}\right)^2 \alpha + C_{L_{\alpha^2}}(\alpha - 6\ \text{deg})_+^2$$

$$\hat{C}_D = C_{D_0} + C_{D_\alpha}\alpha + C_{D_{\delta_e}}\delta_e + C_{D_X}(1-X) + C_{D_{C_T}}C_T$$

$$\hat{C}_Y = C_{Y_0} + C_{Y_\beta}\beta + C_{Y_p}\frac{p\bar{b}}{2V} + C_{Y_r}\frac{r\bar{b}}{2V} + C_{Y_{\delta_a}}\delta_a$$

$$\hat{C}_l = C_{l_0} + C_{l_\beta}\beta + C_{l_p}\frac{p\bar{b}}{2V} + C_{l_r}\frac{r\bar{b}}{2V} + C_{l_{\delta_a}}\delta_a$$

$$\hat{C}_m = C_{m_0} + C_{m_\alpha}\alpha + C_{m_{X\delta_e}}\max\left(\frac{1}{2}, X\right)\delta_e + C_{m_{C_T}}C_T$$

$$\hat{C}_n = C_{n_0} + C_{n_\beta}\beta + C_{n_r}\frac{r\bar{b}}{2V} + C_{n_{\delta_r}}\delta_r \tag{41}$$

2. *Parameter Estimation*

As explained in Sec. II.A.4, in our approach, the flow separation model (X) parameters τ_1, τ_2, a_1, and α^* were estimated in an iterative scheme for model structure selection. The final X parameters were obtained using the final converged C_L model structure, as listed in Eq. (41). The results of this optimization are presented in this section. Figure 18 shows the parameter estimates obtained from the 27 identification datasets. The median estimated parameter values across all datasets were taken as the final parameter estimates $\hat{\theta}$ and are listed in Table 5. In Fig. 18, the figures on the diagonal represent histograms of each estimated parameter, while the off-diagonal graphs show scatterplots of all X-parameter combinations. In the off-diagonal figures, the red star marks the median ($\hat{\theta}$), and correlation coefficient values (ρ) are indicated. Table 5 further lists the upper and lower bounds (θ_{ub} and θ_{lb}) used in the optimization, the spread $[\sigma(\hat{\theta})]$ across the 27 estimates for each parameter, and the results of a one-sample t test (p-value and test decision h) performed to verify if estimated parameter values were statistically different from zero. For the t tests, a Bonferroni correction was applied to adjust the significance level for performing multiple comparisons.

Across the 27 training datasets, Fig. 18 shows consistent X-parameter estimation results, without strong correlations between parameters. For τ_1, a_1, and α^*, the parameter estimate distributions can also be considered normally distributed (see Fig. 18), and the standard deviation across the estimated values (σ) is considerably smaller than the average estimated value. For τ_2, the skewed distribution and large spread are indicative of reduced accuracy in the estimation of this parameter. Still, as shown in Table 5, one-sample

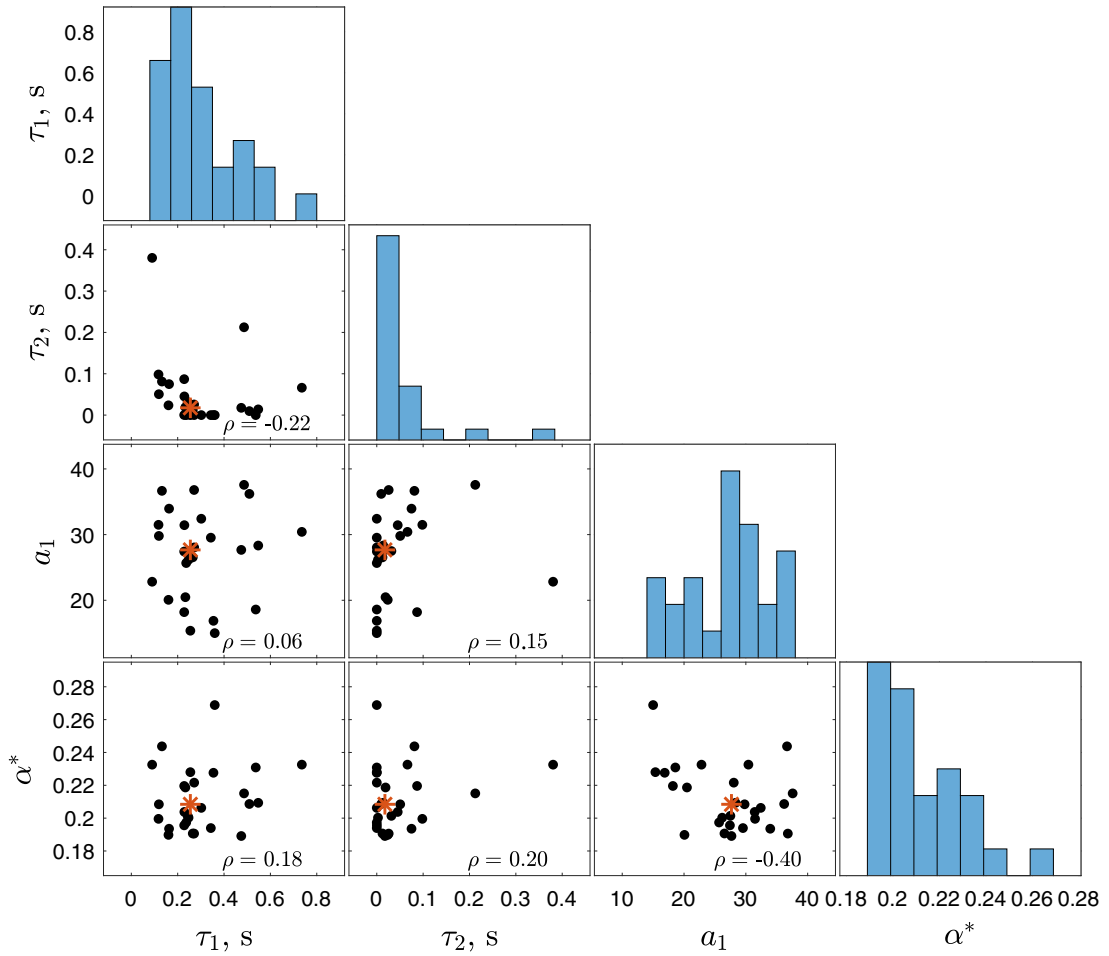

Fig. 18 Matrix plot of the estimated X parameters.

Table 5 Estimated X-parameter values and one-sample t-test results

Parameter		Results				t test	
Name	Unit	$\hat{\theta}$	θ_{lb}	θ_{ub}	$\sigma(\hat{\theta})$	p	h
τ_1	s	0.2547	0.001	0.80	0.1565	0.000	*
τ_2	s	0.0176	0.000	0.50	0.0819	0.002	*
a_1	—	27.6711	15.000	40.00	6.7177	0.000	*
α^*	rad	0.2084	0.100	0.35	0.0202	0.000	*

*Indicates a statistically significant result.

t tests performed to verify if estimated parameter values were statistically different from zero confirmed this for all X parameters, including τ_2.

Furthermore, Table 6 compares the estimated X parameters for the Cessna Citation II with values reported for other aircraft in literature [47,78]. Note that for this comparison, the τ_1 and τ_2 time constants are made dimensionless. The estimated a_1 and α^* values were found to be consistent with estimates for the other aircraft types. However, our estimated τ_1 and τ_2 are comparatively lower, a factor of 2 and 5, respectively, compared to the comparison aircraft in Table 6. Overall, a lower accuracy of the τ_1 and τ_2 estimates was not unexpected and can be considered a direct result of the quasi-steady stalls performed in the flight tests (see Sec. III). As illustrated in Fig. 19, while the static parameters a_1 and α^* influence the modeled C_L throughout the considered stall maneuver, the effect of variations in τ_1 and τ_2 is only limited. These parameters are essential for modeling deep aerodynamic stalls, with the flow (re-)attachment and hysteresis effects that occur then but not fully excited in (benign) quasi-steady stall maneuvers.

Table 6 Comparison of estimated X-parameter values to literature (for Cessna Citation II: $\bar{c} = 2.06$ m and $V_{stall} \approx 75$ m/s)

Parameter	Citation II	VFW-614 [47]	C-160 [47]	AT-26 [78]
$\tau_1 \frac{V}{\bar{c}}$	9.27	15.6	14.5	—
$\tau_2 \frac{V}{\bar{c}}$	0.64	4.45	3.46	—
a_1	27.67	15.00	25.70	25.00
α^*, rad	0.21	0.34	0.36	0.25

In the same format as Fig. 18, Fig. 20 shows the estimated values for the three coefficients (C_{L_0}, C_{L_α}, and $C_{L_{\alpha^2}}$) of the identified C_L model structure; see Eq. (41). Similar results for the other aerodynamic force and moment coefficients are not included here for brevity but are reported in [29]. Figure 20 shows that the estimated bias and α coefficients are strongly negatively correlated ($\rho = -0.9$). This is a direct result of the segments of flight-test data (e.g., see Fig. 21) used for model identification, which intentionally included considerable stretches of normal (unstalled) flight prior to and following the stall. While this ensures that the aerodynamic coefficient values for our stall model remain consistent with parameter values estimated from nominal flight, it is unavoidable that during these (considerable) parts of the identification data the angle of attack is approximately constant. While this constant α causes C_{L_0} and C_{L_α} to be somewhat interchangeable and thus correlated, removing either of these parameters results in a strong increase in modeling errors. Similar observations were made for the C_D and C_m modeling results in [29].

3. *Model Validation*

In [29], seven of the available 34 flight-test datasets were used for model validation (80–20 split). Table 7 lists the MSE and the

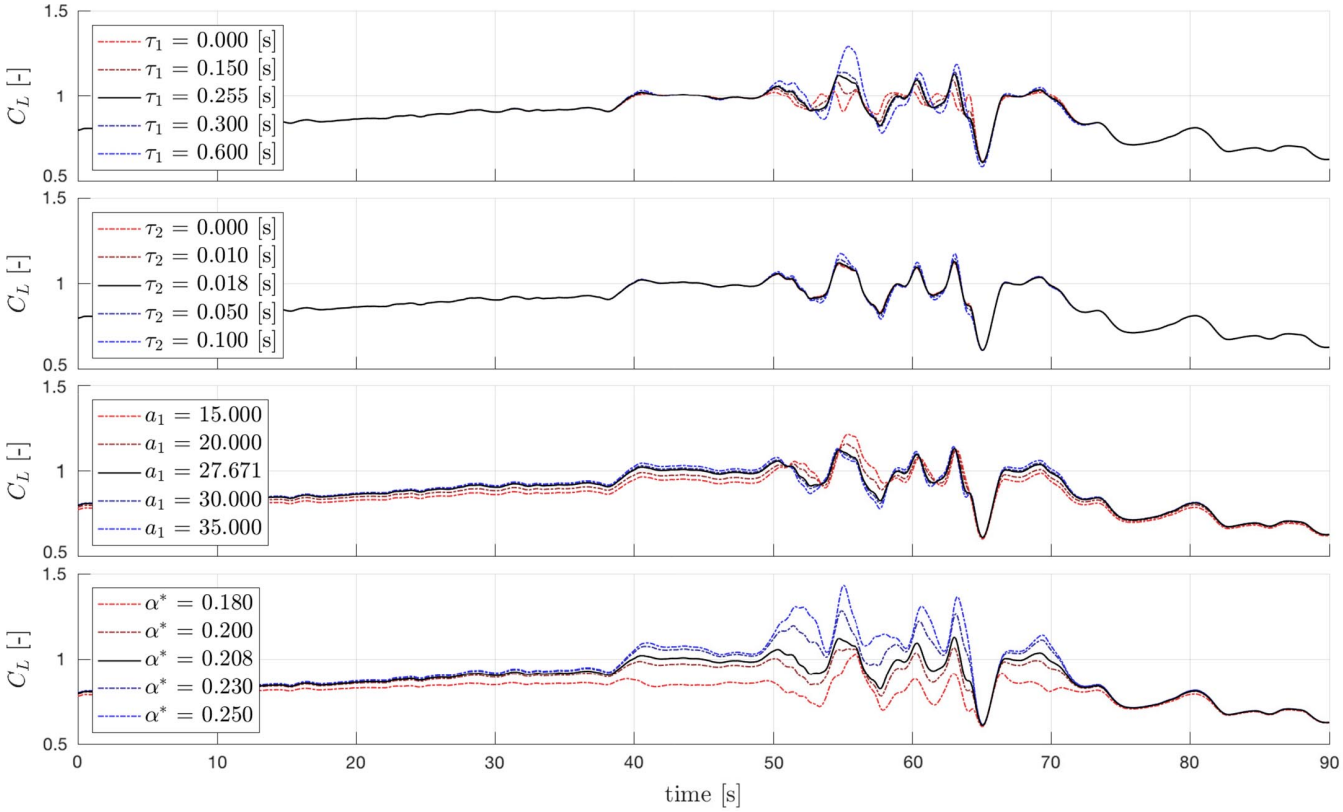

Fig. 19 Visualization of the sensitivity of the model output to the *X* parameters; whereas the static parameters influence almost the entire time history, the dynamic parameters only affect the part where the aircraft actually stalls; dataset 3 (training) is shown.

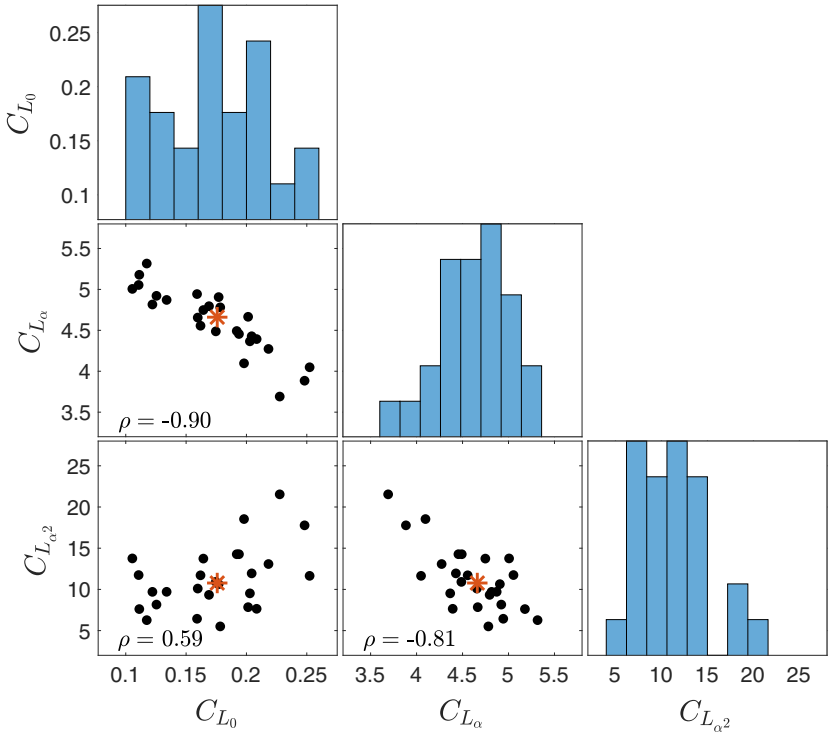

Fig. 20 Matrix plot of the estimated C_L parameters.

coefficient of determination (R^2) for both the training and validation data. Time histories comparing model output to measured data for three selected validation datasets, representing the best-, average-, and worst-quality fit, are shown in Fig. 21.

Figure 21 shows good agreement of the fitted models with the flight-test data, also during the stall. There are some stall-related effects that are not reflected by the model, for instance in the C_L and C_D time histories of the "average" plot in Fig. 21. However, the model realigns with the data once the aircraft recovers from the stall. Furthermore, model quality is approximately the same on the training and validation sets (see Table 7), which suggests no issues occur with under- or overfitting and the effectiveness of the used

Table 7 Fit quality metrics for training and validation data [29]

	Training data (27 sets)				Validation data (seven sets)			
Coefficient	MSE	R^2	Min (R^2)	Max (R^2)	MSE	R^2	Min (R^2)	Max (R^2)
C_L	1.65×10^{-3}	0.92	0.71	0.98	1.45×10^{-3}	0.91	0.77	0.96
C_D	1.01×10^{-4}	0.74	−1.47	0.97	6.72×10^{-5}	0.89	0.84	0.94
C_Y	4.68×10^{-5}	0.66	−0.67	0.91	4.55×10^{-5}	0.57	0.29	0.82
C_l	2.40×10^{-6}	0.54	−0.60	0.85	1.97×10^{-6}	0.47	0.08	0.92
C_m	9.93×10^{-5}	0.68	−0.39	0.92	9.87×10^{-5}	0.73	0.26	0.92
C_n	8.21×10^{-7}	0.49	−0.66	0.96	8.66×10^{-7}	0.12	−0.43	0.80

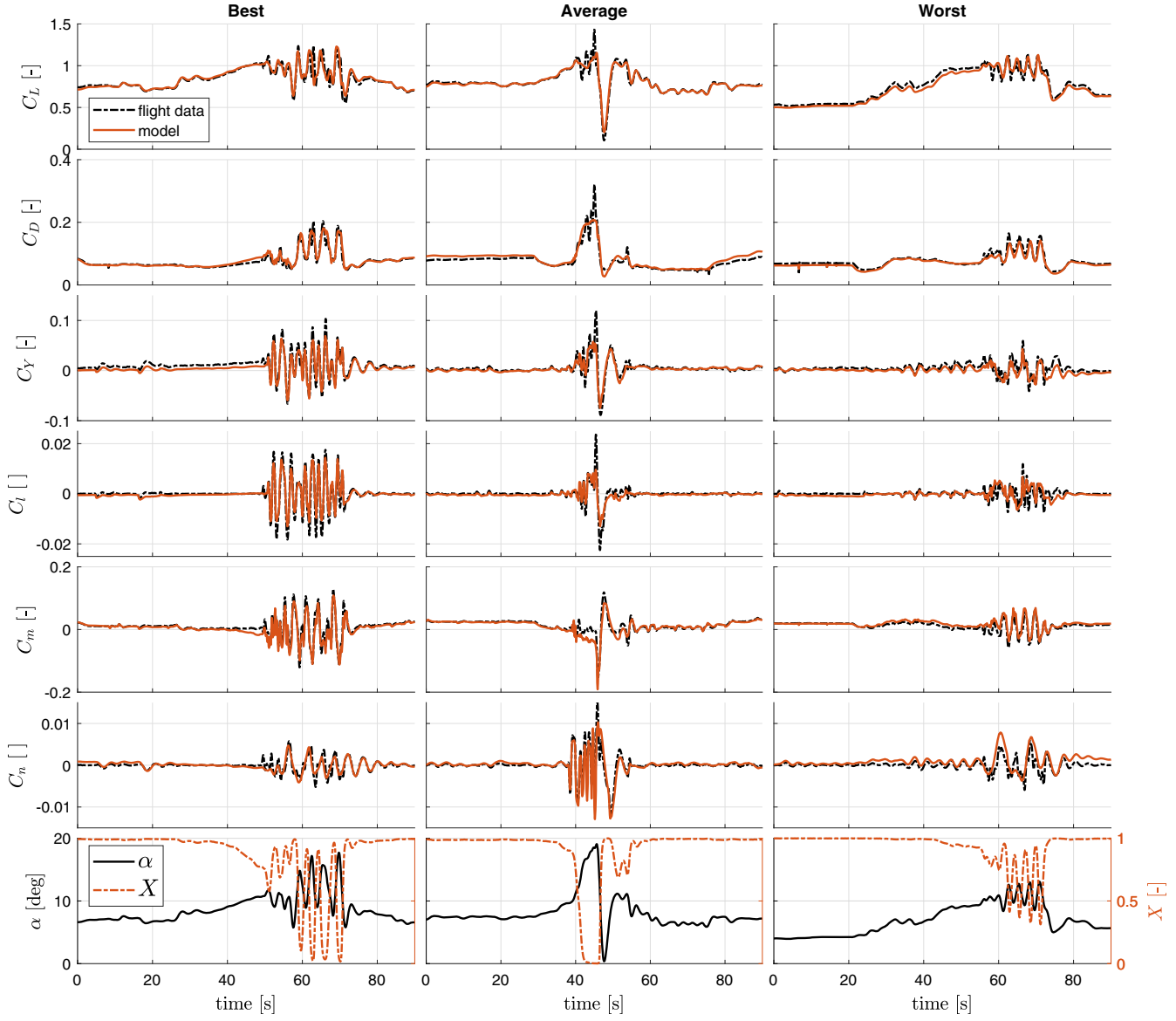

Fig. 21 Model validation results for three levels of validation fit quality (best/average/worst) [29]; the bottom figure shows the corresponding angle of attack and the flow separation state X.

model identification and model structure selection. The min(R^2) columns in Table 7 show that for some of the asymmetric models (lateral force, roll, and yaw), negative R^2 values were found. This is explained by the lacking excitation of the lateral aircraft dynamics present in some of the (symmetrical) stall datasets (see Sec. III), for which the identified model was found to overpredict the corresponding force or moment coefficient changes.

C. Model-Based Control

Multivariate spline-based aerodynamic models open up new possibilities in nonlinear model-based control of aircraft with highly nonlinear aerodynamics. Not only does the control performance improve due to a potentially smaller mismatch between reality and the model, but also analytical (directional) derivatives are readily available, smoothness is guaranteed, and bounds on model quality

can be provided. In [79], the first multivariate simplex B-spline-based nonlinear dynamic inversion controller was applied on a simulation of the F-16 fighter aircraft. In [32], this approach was made adaptive by using a recursive multivariate simplex B-spline estimator to compensate for aerodynamic uncertainties. In [33], a novel INCA approach was presented that is suitable for use with non-control affine systems with nonlinear state–effector and effector–effector interactions for the ICE aircraft. The INCA approach is made possible by an internal (analytical) multivariate spline-based control effectiveness model.

Consider the following non-affine system dynamics:

$$\dot{\boldsymbol{x}} = \boldsymbol{F}(\boldsymbol{x}) + \boldsymbol{\Phi}(\boldsymbol{x}, \boldsymbol{u}) \tag{42}$$

where $\boldsymbol{F}(\boldsymbol{x})$ contains purely aerodynamic forces and moments not produced by the control effectors, and with $\boldsymbol{\Phi}(\boldsymbol{x}, \boldsymbol{u})$ the nonlinear, non-affine control effector model, which may contain state–effector and effector–effector interactions. The INCA approach is an incremental control approach [80] with accompanying assumptions (see [81] for an in-depth discussion), and hence computes actuator position increments $\Delta\boldsymbol{u}$, which are added to the current actuator positions $\boldsymbol{u}_0$ to reach the absolute effector position command: $\boldsymbol{u} = \boldsymbol{u}_0 + \Delta\boldsymbol{u}$. In incremental form, Eq. (42) reduces to

$$\dot{\boldsymbol{x}} \approx \dot{\boldsymbol{x}}_0 + \nabla_u \boldsymbol{\Phi}(\boldsymbol{x}, \boldsymbol{u}) \Delta\boldsymbol{u} \tag{43}$$

with $\dot{\boldsymbol{x}}_0$ the current state derivative, which is either directly measured using (angular) accelerometers or derived from rate measurements. In Eq. (43), the control effectiveness Jacobian (CEJ) $\nabla_u \boldsymbol{\Phi}(\boldsymbol{x}, \boldsymbol{u})$ is defined as follows:

$$\nabla_u \boldsymbol{\Phi}(\boldsymbol{x}, \boldsymbol{u}) = \frac{\partial \boldsymbol{\Phi}(\boldsymbol{x}, \boldsymbol{u})}{\partial \boldsymbol{u}} \in \mathbb{R}^{n \times m}, \quad m > n \tag{44}$$

where the CEJ is not invertible for an overactuated system. In the case of the ICE aircraft, the CEJ from Eq. (44) is derived analytically from the multivariate spline-based aerodynamic moment models S_{l_j}, S_{m_j}, and S_{n_j} from Eq. (39) using the methodology from [63]. This yields 13 analytical partial derivatives for each of the 108 spline models with which the CEJ matrix for the ICE aircraft is constructed as follows:

$$\nabla_u \boldsymbol{\Phi}(\boldsymbol{x}, \boldsymbol{u}) = \begin{bmatrix} \sum_{j=1}^{20} \frac{\partial S_{l_j}(\boldsymbol{x}, \boldsymbol{u})}{\partial \delta_1} & \sum_{j=1}^{20} \frac{\partial S_{l_j}(\boldsymbol{x}, \boldsymbol{u})}{\partial \delta_2} & \cdots & \sum_{j=1}^{20} \frac{\partial S_{l_j}(\boldsymbol{x}, \boldsymbol{u})}{\partial \delta_{13}} \\ \sum_{j=1}^{20} \frac{\partial S_{m_j}(\boldsymbol{x}, \boldsymbol{u})}{\partial \delta_1} & \sum_{j=1}^{20} \frac{\partial S_{m_j}(\boldsymbol{x}, \boldsymbol{u})}{\partial \delta_2} & \cdots & \sum_{j=1}^{20} \frac{\partial S_{m_j}(\boldsymbol{x}, \boldsymbol{u})}{\partial \delta_{13}} \\ \sum_{j=1}^{20} \frac{\partial S_{n_j}(\boldsymbol{x}, \boldsymbol{u})}{\partial \delta_1} & \sum_{j=1}^{20} \frac{\partial S_{n_j}(\boldsymbol{x}, \boldsymbol{u})}{\partial \delta_2} & \cdots & \sum_{j=1}^{20} \frac{\partial S_{n_j}(\boldsymbol{x}, \boldsymbol{u})}{\partial \delta_{13}} \end{bmatrix} \tag{45}$$

Each element in Eq. (45) is itself a continuous multivariate B-spline function, which is locally evaluated at the current state $\boldsymbol{x}$ and input $\boldsymbol{u}$ at each time step; no separate interpolation schemes are required, which improves both transparency and execution performance. The local nature of the multivariate spline basis functions results in highly efficient evaluation routines, as the CEJ only needs to be evaluated on a single simplex for each of the 108 submodels at every time step. The result is that >90,000 complete CEJ evaluations per second can be performed for the C^0 continuous model and >10,000 per second for the C^1 model, both on a single CPU core of desktop computer (AMD Ryzen 9 5900X at 3.7 GHz).

The INCA optimization problem is then formulated as follows: given the current state $\boldsymbol{x}_0$, the current actuator positions $\boldsymbol{u}_0$, acceleration measurements $\dot{\boldsymbol{x}}_0$ (if available, and acceleration estimations if not; see, e.g., [80]), and a pseudocontrol input command $\boldsymbol{d}_c = [\boldsymbol{\nu}(\boldsymbol{x}) - \dot{\boldsymbol{x}}_0]$, determine an increment in the control input vector $\Delta\boldsymbol{u}$ such that

$$\begin{aligned} &\nabla_u \boldsymbol{\Phi}(\boldsymbol{x}_0, \boldsymbol{u}_0)\, \Delta\boldsymbol{u} = \boldsymbol{d}_c \\ &\text{subject to} \quad \underline{\Delta\boldsymbol{u}} \le \Delta\boldsymbol{u} \le \overline{\Delta\boldsymbol{u}} \end{aligned} \tag{46}$$

where $\underline{\Delta\boldsymbol{u}}$ and $\overline{\Delta\boldsymbol{u}}$ are the most restrictive upper and lower bounds on the actuator rates, as well as actuator position limits, translated into local incremental constraints.

Next to solving Eq. (46) with an easy-to-implement pseudo-inverse-based approach, it can also be solved as a numerical optimization problem with explicit constraints. A common approach formulates the control allocation problem as a multi-objective constrained optimization problem, solved as a quadratic program:

$$\begin{aligned} &\min_{\Delta u} \; \mathcal{J} = W_d \| \nabla_u \Phi(\boldsymbol{x}, \boldsymbol{u}) \Delta\boldsymbol{u} - \boldsymbol{d}_c \|_2^2 + \eta W_u \| f(\boldsymbol{x}, \boldsymbol{u}) \|_2^2 \\ &\text{subject to} \;\; \underline{\boldsymbol{u}} \le \boldsymbol{u} \le \overline{\boldsymbol{u}}, \; \underline{\Delta\boldsymbol{u}} \le \Delta\boldsymbol{u} \le \overline{\Delta\boldsymbol{u}} \end{aligned} \tag{47}$$

where η is a scalar, selected sufficiently small to prioritize the minimization of the allocation error over the secondary objectives, and W_d and W_u are nonsingular weighting matrices that are tunable by the user, and with $f(\boldsymbol{x}, \boldsymbol{u})$ a secondary objective function (e.g., aircraft drag and/or desired actuator positions). The optimization problem from Eq. (47) can be solved effectively using the active set algorithm described in [82]. In Fig. 22, the tracking performance of INCA is compared to a linear control allocation (LCA) approach employing a redistributed weighted pseudo-inverse optimization, in which the CEJ in Eq. (42) is linearized over the flight envelope. Clearly, the tracking performance of INCA is superior to the LCA, with the LCA at some stages suffering from significant excursions from the reference trajectory. In Fig. 23, the respective control effector deflections are compared, showing that INCA effector deflections are comparable in magnitude to the LCA deflections. This demonstrates that INCA with the multivariate spline-based CEJ is better able to exploit state–effector and effector–effector interactions than the LCA approach.

D. Model Parameter Tolerances

Next to direct applications of improved models of aircraft flight dynamics, a focus of our research has also been to investigate how accurate such models in fact need to be. For example, since 2019, it has become obligatory for airline pilots to receive stall training in flight simulators [3,5,83,84]. As a result, new stall and poststall dynamic models were developed for use in flight simulators. However, as of yet current regulatory standards for stall model accuracy in simulators used for pilot training, both for the stall aerodynamics and stall buffet, reflect persistent uncertainty regarding the required level of model fidelity for sufficiently accurate stall simulations and effective pilot training [4,85].

To address this issue, we have performed a number of flight simulator experiments in Delft University of Technology's SRS (see Figs. 24a and 24b) to provide quantitative guidance on the required accuracy of simulated stall dynamics [34] and stall buffet characteristics [35] in flight simulators. In these experiments, minimum safe requirements on key model parameters were determined by measuring their just noticeable difference (JND) thresholds (i.e., the largest allowable offset in the parameter value that could be noticed by pilots in the simulator). To measure these JND thresholds, we use a experimental paradigm (see Fig. 24c), where a participating pilot experiences simulated stall maneuvers as an observer. Through psycho-physical experiments with a subjective staircase procedure, consisting of repeated pairwise comparisons of a stall with the true "baseline" model parameter setting and a stall with an "offset" parameter setting, the JND thresholds for individual model parameters can be determined.

Figure 24d shows an overview of the experimental results obtained for the flow separation model parameters τ_1 (lower and upper JND) and a_1 (lower and upper JND) in [34], as well as results from [35] for the stall buffet model parameters X_{thres} (only lower JND) and ω_0 (upper and lower JND). These results were obtained from type-licensed Citation II pilots, as well as other (commercial, private, or glider) pilots. The right vertical axes in all figures indicate the measured JND in terms of the Weber fraction (i.e., the maximum allowable percentage-wise offset in parameter value). While these results indicate that small parameter offsets indeed are unlikely to be

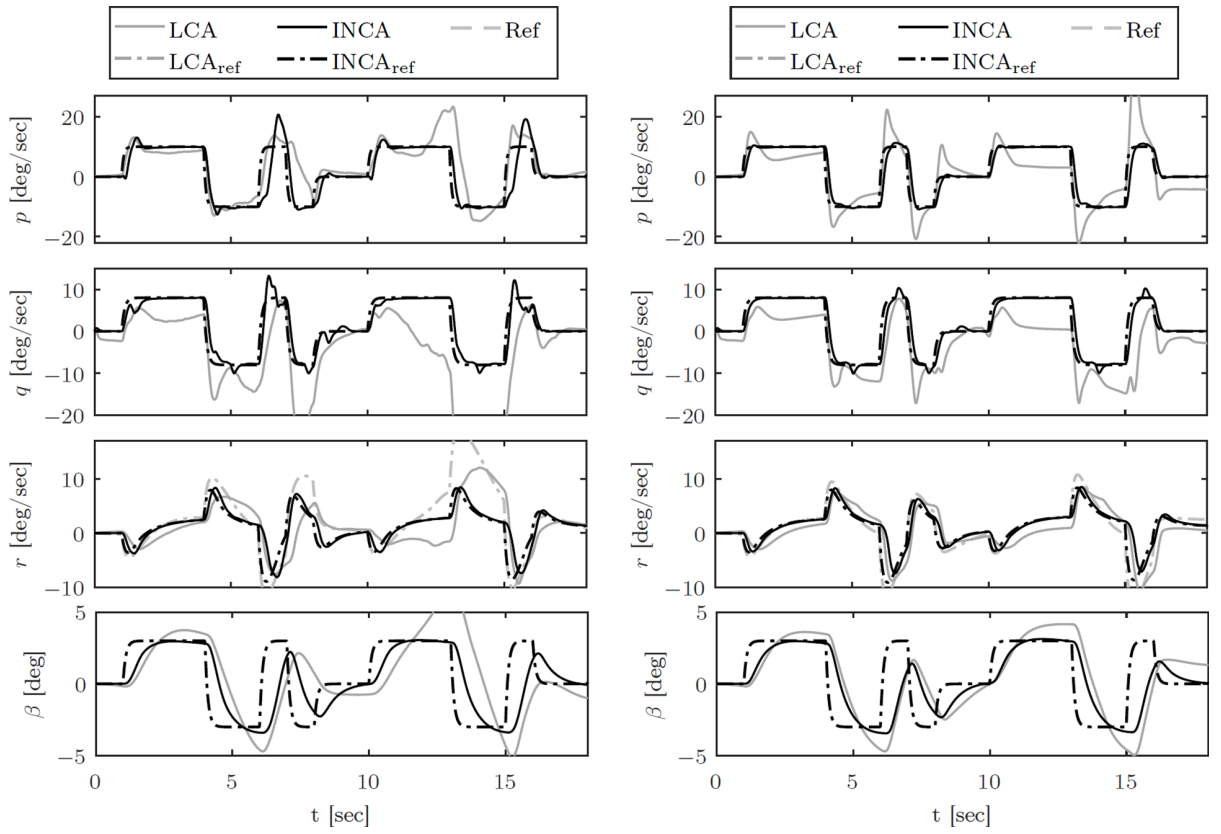

Fig. 22 Comparison of tracking performance of INCA and an LCA approach for a coupled 3211 maneuver on both q and p.

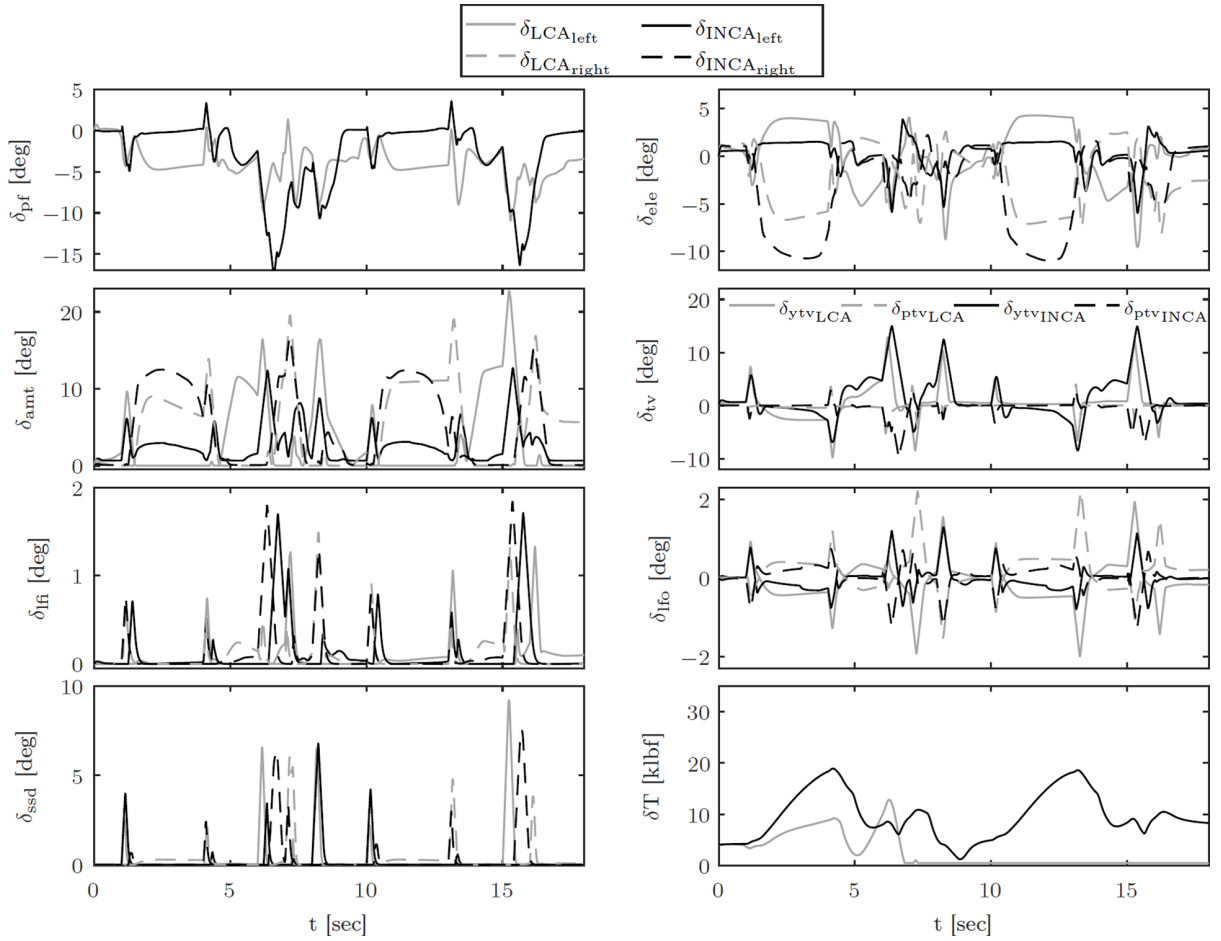

Fig. 23 Comparison of control effector deflections resulting from INCA and an LCA approach for a coupled 3211 maneuver on both q and p; pf = pitch flap, am t = all moving tip, lfi = inboard leading-edge flap, lfo = outboard leading-edge flap, ss d = spoiler–slot–deflector, ele = elevons, tv = thrust vector, and δT = engine thrust.

a) SIMONA Research Simulator

b) Simulator cockpit

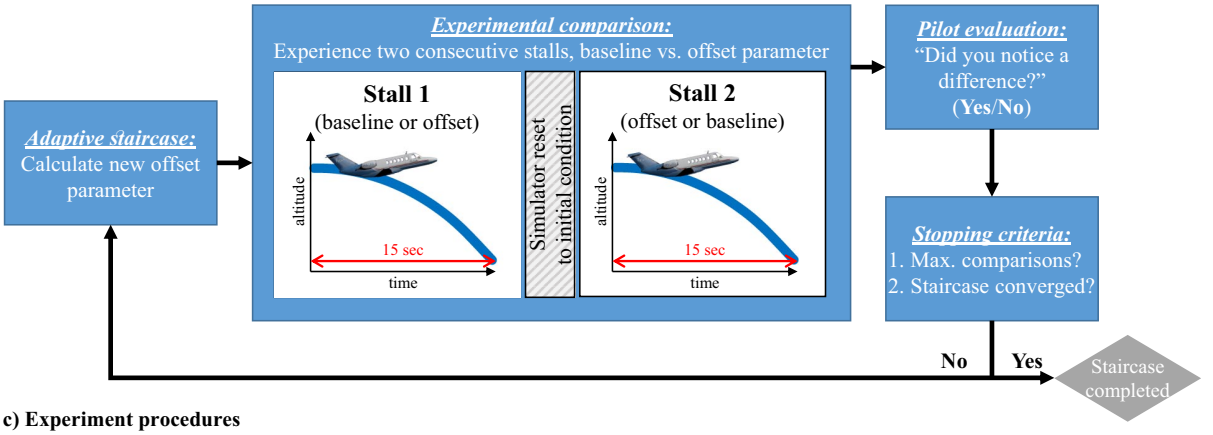

c) Experiment procedures

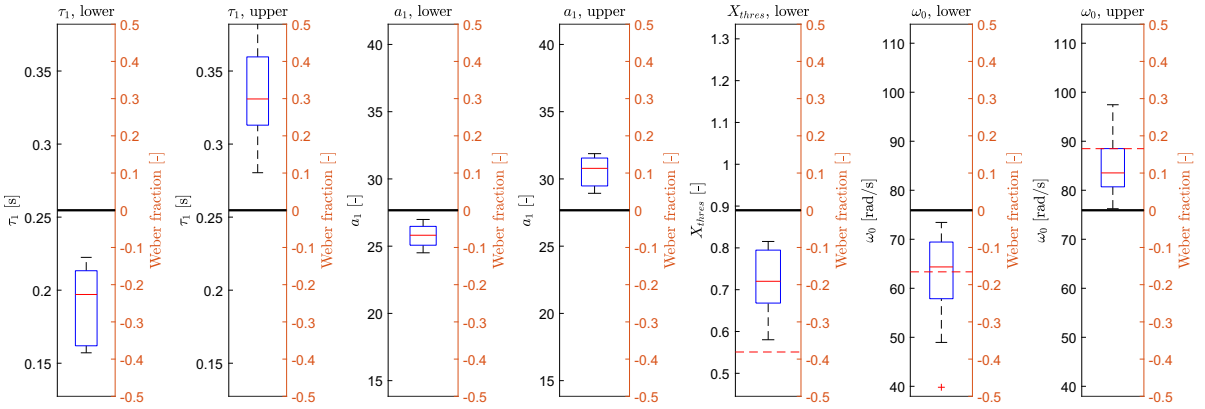

d) JND threshold results from [35] and [36]

Fig. 24 Overview of stall model parameter tolerance flight simulator experiments.

noticed by pilots on average, Fig. 24d shows that even parameter offsets of 10% or less (e.g., a_1) may already result in differences that are noticeable for pilots. In our view, such results indicate that human pilots' capacity for noticing differences in simulated aircraft dynamics should be taken into account when accepted maximum modeling tolerances are defined.

V. Conclusions

This paper provides an (incomplete) overview of current research on flight testing and model identification at the authors' research group at Delft University of Technology, focusing only on methods, (numerical) experiments, and outcomes obtained for Delft University of Technology's Cessna Citation II laboratory aircraft, and the Lockheed Martin Innovative Control Effector demonstrator. The presented work on nonlinear stall model identification and aerodynamic modeling with multivariate B-splines shows the importance of synergy between identification and modeling methods, flight-test experiments, and modeling results and applications for focusing research activities and achieving structural progress. For example, the required accuracy of new models of aircraft stall dynamics for simulator-based pilot training, as well as the identification methods to obtain them, should be based on pilots' sensitivity to variations in identified model parameters but perhaps not for better efficiency. Focused identification inputs during flight testing and objective model structure selection approaches are found to be invaluable for

reliable estimated model parameters and valid aerodynamic modeling results. Novel control approaches, such as the INCA method, cannot be implemented with traditional aerodynamic model structures (e.g., simple polynomials), but they require new approaches for implementing nonlinear state-varying aerodynamic coefficients, such as multivariate simplex B-spline-based models.

With the current emphasis on drones and revolutionary new aircraft concepts aimed at reducing the environmental impact of aviation and/or realize our visions for UAM, the importance of the field of flight testing and model identification will only grow in the years to come. There will be more demand for models in design processes and as integral parts of onboard control systems and ground-based simulation facilities. Especially, given the increasing nonlinearity of the aerodynamics governing many of these new aerial vehicles, the recent lessons learned from traditional fixed-wing flight testing and aerodynamic modeling that have also focused increasingly more on nonlinear effects (e.g., stall) will be of great benefit. Going beyond the "stalls and splines," as summarized in this paper, the section of C&S of the Faculty of Aerospace Engineering at Delft University of Technology will continue to contribute to this crucial topic in aerospace engineering.

Acknowledgments

The authors would like to thank the following alumni of the Delft University of Technology for their contributions to developing the multivariate simplex B-spline method for aerodynamic model identification: Elisabeth Brunner, Liguo Sun, Henry Tol, Tim Visser, Florian Huisman, Johann Meyer, Ivo van der Peijl, Marc van den Aarssen, Ismael Matamoros, Giliam Datema, and Lukas Steiner. The authors thank the following Delft University of Technology alumni for their contributions to experimental methodologies: Sophie Armanini, Joao Caetano, Sihao Sun, Jasper van Beers, Karan Vir Bains, Prashant Solanki, Mathias Baert, Bram Strack van Schijndel, Vimarsh Joshi, and Frank Rijks. The authors also thank the following (former) M.Sc. students for their contributions to the stall modeling research: Patrick Brill, Arne Imbrechts, Peter Luteijn, Alexandre Delfosse, Emma de Meester, Sven Marschalk, Stephan Smets, Joost van Ingen, Laurens van Horssen, and Marlon van den Hoek. Finally, the authors owe great thanks to Alexander in 't Veld, Hans Mulder, Andries Muis, Ferdinand Postema, Fred den Toom, and Menno Klaassen for their invaluable help in realizing the flight-test experiments.

References

[1] Anon., "Code of Federal Regulations, Title 14, Part 60: Flight Simulation Training Device Initial and Continuing Qualification and Use," 2016, https://www.ecfr.gov/current/title-14/chapter-I/subchapter-D/part-60 [retrieved 7 May 2023].

[2] Anon., "Stall and Stick Pusher Training," Advisory Circular 120-109, U.S. Department of Transportation, Federal Aviation Administration, Aug. 2012, https://www.faa.gov/documentlibrary/media/advisory_circular/ac%20120-109.pdf [retrieved 8 June 2023].

[3] Advani, S. K., and Schroeder, J. A., "Global Implementation of Upset Prevention & Recovery Training," *AIAA Modeling and Simulation Technologies Conference*, AIAA Paper 2016-1430, Jan. 2016. https://doi.org/10.2514/6.2016-1430

[4] Advani, S. K., and Field, J., "Upset Prevention and Recovery Training in Flight Simulators," *AIAA Modeling and Simulation Technologies Conference*, AIAA Paper 2011-6698, Aug. 2011. https://doi.org/10.2514/6.2011-6698

[5] Schroeder, J. A., "Research and Technology in Support of Upset Prevention and Recovery Training," *AIAA Modeling and Simulation Technologies Conference 2012*, AIAA Paper 2012-4567, Aug. 2012. https://doi.org/10.2514/6.2012-4567

[6] Advani, S. K., Schroeder, J. A., and Burks, B., "What Really Can Be Done in Simulation to Improve Upset Training?" *AIAA Modeling and Simulation Technologies Conference*, AIAA Paper 2010-7791, Aug. 2010. https://doi.org/10.2514/6.2010-7791

[7] Sun, S., and de Visser, C., "Aerodynamic Model Identification of a Quadrotor Subjected to Rotor Failures in the High-Speed Flight Regime," *IEEE Robotics and Automation Letters*, Vol. 4, No. 4, 2019, pp. 3868–3875. https://doi.org/10.1109/LRA.2019.2928758

[8] Sun, S., de Visser, C. C., and Chu, Q., "Quadrotor Gray-Box Model Identification from High-Speed Flight Data," *Journal of Aircraft*, Vol. 56, No. 2, 2019, pp. 645–661. https://doi.org/10.2514/1.C035135

[9] Grauer, J., Ulrich, E., Hubbard, J., Pines, D., and Humbert, J. S., "Testing and System Identification of an Ornithopter in Longitudinal Flight," *Journal of Aircraft*, Vol. 48, No. 2, 2010, pp. 660–667. https://doi.org/10.2514/1.C031208

[10] Karasek, M., Muijres, F. T., De Wagter, C., Remes, B. D., and de Croon, G. C., "A Tailless Aerial Robotic Flapper Reveals that Flies Use Torque Coupling in Rapid Banked Turns," *Science*, Vol. 361, No. 6407, 2018, pp. 1089–1094. https://doi.org/10.1126/SCIENCE.AAT0350

[11] Oosterom, W. J., and Vos, R., "Conceptual Design of a Flying-V Aircraft Family," *AIAA AVIATION 2022 Forum*, AIAA Paper 2022-3200, July 2022. https://doi.org/10.2514/6.2022-3200

[12] Silva, C., Johnson, W., Antcliff, K. R., and Patterson, M. D., "VTOL Urban Air Mobility Concept Vehicles for Technology Development," *2018 Aviation Technology, Integration, and Operations Conference*, AIAA Paper 2018-3847, June 2018. https://doi.org/10.2514/6.2018-3847

[13] Straubinger, A., Rothfeld, R., Shamiyeh, M., Büchter, K. D., Kaiser, J., and Plötner, K. O., "An Overview of Current Research and Developments in Urban Air Mobility—Setting the Scene for UAM Introduction," *Journal of Air Transport Management*, Vol. 87, Aug. 2020, Paper 101852. https://doi.org/10.1016/J.JAIRTRAMAN.2020.101852

[14] Gerlach, O., "The Determination of Stability Derivatives and Performance Characteristics from Dynamic Manoeuvres," *38th Meeting of the AGARD Flight Mechanics Panel*, 1971, p. 45, https://repository.tudelft.nl/islandora/object/uuid%3A135bbe54-719c-4891-82bf-f3a300fdc19b.

[15] Mulder, J. A., Jonkers, H. L., Horsten, J. J., Breeman, J. H., and Simons, J. L., "Analysis of Aircraft Performance, Stability and Control Measurements," AGARD Rept. AGARD-LS-104, 1979, https://apps.dtic.mil/sti/pdfs/ADA081645.pdf#page=97 [retrieved 12 July 2023].

[16] Mulder, J. A., and den Hollander, J. G., "Status of Dynamic Flight Test Technology—Model Identification for Flight Simulation," *SAE Transactions*, Vol. 90, Jan. 1981, pp. 2079–2094, http://www.jstor.org/stable/44632762.

[17] Plaetschke, E., Mulder, J. A., and Breeman, J. H., "Flight Test Results of Five Input Signals for Aircraft Parameter Identification," *IFAC Proceedings Volumes*, Vol. 15, No. 4, 1982, pp. 1149–1154. https://doi.org/10.1016/s1474-6670(17)63152-5

[18] Jong, R. C. D., and Mulder, J. A., "Accurate Estimation of Aircraft Inertia Characteristics from a Single Suspension Experiment," *Journal of Aircraft*, Vol. 24, No. 6, 1987, pp. 362–370. https://doi.org/10.2514/3.45454

[19] Chu, Q. P., Mulder, J. A., and Woerkom, P. T. V., "Modified Recursive Maximum Likelihood Adaptive Filter for Nonlinear Aircraft Flight-Path Reconstruction," *Journal of Guidance, Control, and Dynamics*, Vol. 19, No. 6, 1996, pp. 1285–1295. https://doi.org/10.2514/3.21784

[20] Mulder, J. A., Chu, Q. P., Sridhar, J. K., Breeman, J. H., and Laban, M., "Non-Linear Aircraft Flight Path Reconstruction Review and New Advances," *Progress in Aerospace Sciences*, Vol. 35, No. 7, 1999, pp. 673–726. https://doi.org/10.1016/S0376-0421(99)00005-6

[21] Stroosma, O., van Paassen, M. M., and Mulder, M., "Using the SIMONA Research Simulator for Human-Machine Interaction Research," *AIAA Modeling and Simulation Technologies Conference and Exhibit*, AIAA Paper 2003-5525, Aug. 2003. https://doi.org/10.2514/6.2003-5525

[22] Caetano, J., Visser, C. D., Croon, G. D., Remes, B., Wagter, C. D., Verboom, J., and Mulder, M., "Linear Aerodynamic Model Identification of a Flapping Wing MAV Based on Flight Test Data," *International Journal of Micro Air Vehicles*, Vol. 5, No. 4, 2013, pp. 273–286. https://doi.org/10.1260/1756-8293.5.4.273

[23] Armanini, S., de Visser, C., de Croon, G., and Mulder, M., "Time-Varying Model Identification of Flapping-Wing Vehicle Dynamics Using Flight Data," *Journal of Guidance, Control, and Dynamics*, Vol. 39, No. 3, 2016, pp. 526–541. https://doi.org/10.2514/1.G001470

[24] Armanini, S. F., Caetano, J. V., Croon, G. C., de Visser, C. C., and Mulder, M., "Quasi-Steady Aerodynamic Model of Clap-and-Fling Flapping MAV and Validation Using Free-Flight Data," *Bioinspiration*

& Biomimetics, Vol. 11, No. 4, 2016, Paper 046002.
https://doi.org/10.1088/1748-3190/11/4/046002

[25] Armanini, S. F., Karasek, M., and de Visser, C. C., "Global Linear Parameter-Varying Modeling of Flapping-Wing Dynamics Using Flight Data," *Journal of Guidance, Control, and Dynamics*, Vol. 41, No. 11, 2018, pp. 2338–2360.
https://doi.org/10.2514/1.G003505

[26] Armanini, S., Caetano, J., de Visser, C., Pavel, M., de Croon, G., and Mulder, M., "Modelling Wing Wake and Tail Aerodynamics of a Flapping-Wing Micro Aerial Vehicle," *International Journal of Micro Air Vehicles*, Vol. 11, March 2019, Paper 1756829319833674.
https://doi.org/10.1177/1756829319833674

[27] Grauer, J. A., and Hubbard, J. E., "Development of a Sensor Suite for a Flapping-Wing UAV Platform," AIAA Paper 2008-0224, Jan. 2008.
https://doi.org/10.2514/6.2008-224

[28] Armanini, S., Karasek, M., de Croon, G., and de Visser, C., "Onboard/Offboard Sensor Fusion for High-Fidelity Flapping-Wing Robot Flight Data," *Journal of Guidance, Control, and Dynamics*, Vol. 40, No. 8, 2017, pp. 2121–2132.
https://doi.org/10.2514/1.G002527

[29] van Ingen, J. B., de Visser, C. C., and Pool, D. M., "Stall Model Identification of a Cessna Citation II from Flight Test Data Using Orthogonal Model Structure Selection," *AIAA Modeling and Simulation Technologies Conference*, AIAA Paper 2021-1725, Jan. 2021.
https://doi.org/10.2514/6.2021-1725

[30] de Visser, C. C., "Global Nonlinear Model Identification with Multivariate Splines," Ph.D. Thesis, Faculty of Aerospace Engineering, Delft Univ. of Technology, Delft, The Netherlands, 2011, http://resolver.tudelft.nl/uuid:6bc0134a-0715-4829-903d-6479c5735913.

[31] van Horssen, L. J., de Visser, C. C., and Pool, D. M., "Aerodynamic Stall and Buffet Modeling for the Cessna Citation II Based on Flight Test Data," *AIAA Modeling and Simulation Technologies Conference*, AIAA Paper 2018-1167, Jan. 2018.
https://doi.org/10.2514/6.2018-1167

[32] Tol, H. J., de Visser, C. C., and Kotsonis, M., "Model Reduction of Parabolic PDEs Using Multivariate Splines," *International Journal of Control*, Vol. 91, No. 1, 2019, pp. 175–190.

[33] Matamoros, I., and de Visser, C. C., "Incremental Nonlinear Control Allocation for a Tailless Aircraft with Innovative Control Effectors," *AIAA Guidance, Navigation, and Control Conference*, AIAA Paper 2018-1116, Jan. 2018.
https://doi.org/10.2514/6.2018-1116

[34] Smets, S. C. E., de Visser, C. C., and Pool, D. M., "Subjective Noticeability of Variations in Quasi-Steady Aerodynamic Stall Dynamics," *AIAA Modeling and Simulation Technologies Conference*, AIAA Paper 2019-1485, Jan. 2019.
https://doi.org/10.2514/6.2019-1485

[35] Imbrechts, A., de Visser, C. C., and Pool, D. M., "Just Noticeable Differences for Variations in Quasi-Steady Stall Buffet Model Parameters," *2022 AIAA SciTech Forum*, AIAA Paper 2022-0510, Dec. 2021.
https://doi.org/10.2514/6.2022-0510

[36] de Visser, C. C., Chu, Q. P., and Mulder, J. A., "A New Approach to Linear Regression with Multivariate Splines," *Automatica*, Vol. 45, No. 12, 2009, pp. 2903–2909.

[37] Goman, M. G., and Khrabrov, A. N., "State-Space Representation of Aerodynamic Characteristics of an Aircraft at High Angles of Attack," *Astrodynamics Conference*, AIAA Paper 1992-4651, Aug. 1992.
https://doi.org/10.2514/6.1992-4651

[38] Fischenberg, D., and Jategaonkar, R. V., "Identification of Aircraft Stall Behavior from Flight Test Data," *RTO SCI Symposium on System Identification for Integrated Aircraft Development and Flight Testing*, 1998, http://www.dtic.mil/cgi-bin/GetTRDoc?AD=ADA361699#page=228.

[39] Dias, J. N., "Unsteady and Post-Stall Model Identification Using Dynamic Stall Maneuvers," *AIAA Atmospheric Flight Mechanics Conference*, AIAA Paper 2015-2705, June 2015.
https://doi.org/10.2514/6.2015-2705

[40] Singh, J., and Jategaonkar, R. V., "Identification of Lateral–Directional Behavior in Stall from Flight Data," *Journal of Aircraft*, Vol. 33, No. 3, 1996, pp. 627–630.
https://doi.org/10.2514/3.46993

[41] Delfosse, A., de Visser, C. C., and Pool, D. M., "Asymmetric Stall Modeling of the Cessna Citation II Aircraft," *Proceedings of the 2022 CEAS EuroGNC Conference on Guidance, Navigation and Control*, Council of European Aerospace Societies (CEAS), CEAS-GNC-2022-011, 2022, pp. 1–28.

[42] Lemley, C., and Mullans, R., "Buffeting Pressures on a Swept Wing in Transonic Flight—Comparison of Model and Full Scale Measurements," *Dynamics Specialists Conference*, AIAA Paper 1973-0311, March 1973.
https://doi.org/10.2514/6.1973-311

[43] Caruana, D., Mignosi, A., Corrège, M., Le Pourhiet, A., and Rodde, A. M., "Buffet and Buffeting Control in Transonic Flow," *Aerospace Science and Technology*, Vol. 9, No. 7, 2005, pp. 605–616.
https://doi.org/10.1016/j.ast.2004.12.005

[44] Marschalk, S., Luteijn, P. C., van Os, D., Pool, D. M., and de Visser, C. C., "Stall Buffet Modeling Using Swept Wing Flight Test Data," *2021 AIAA SciTech Forum*, AIAA Paper 2021-0286, Jan. 2021.
https://doi.org/10.2514/6.2021-0286

[45] Morelli, E. A., Cunningham, K., and Hill, M. A., "Global Aerodynamic Modeling for Stall/Upset Recovery Training Using Efficient Piloted Flight Test Techniques," *AIAA Modeling and Simulation Technologies (MST) Conference*, Vol. 308, AIAA Paper 2013-4976, Aug. 2013.
https://doi.org/10.2514/6.2013-4976

[46] Grauer, J. A., and Morelli, E. A., "Generic Global Aerodynamic Model for Aircraft," *Journal of Aircraft*, Vol. 52, No. 1, 2015, pp. 13–20.
https://doi.org/10.2514/1.C032888

[47] Fischenberg, D., "Identification of an Unsteady Aerodynamic Stall Model from Flight Test Data," *20th Atmospheric Flight Mechanics Conference*, AIAA Paper 1995-3438, Aug. 1995, pp. 138–146.

[48] de Visser, C., Mulder, J., and Chu, Q., "Global Nonlinear Aerodynamic Model Identification with Multivariate Splines," *AIAA Atmospheric Flight Mechanics Conference*, AIAA Paper 2009-5726, Aug. 2009.

[49] de Visser, C., Mulder, J. A., and Chu, Q. P., "A Multidimensional Spline Based Global Nonlinear Aerodynamic Model for the Cessna Citation II," *AIAA Atmospheric Flight Mechanics Conference*, AIAA Paper 2010-7950, Aug. 2010.

[50] van den Aarssen, M. S., Visser, T., and de Visser, C. C., "Distributed Approach for Aerodynamic Model Identification of the ICE Aircraft Using the Alternating Direction Method of Multipliers in Combination with Simplotope B-Splines," *AIAA SciTech 2019 Forum*, AIAA Paper 2019-1320, Jan. 2019.
https://doi.org/10.2514/6.2019-1320

[51] Tischler, M. B., and Tobias, E. L., "A Model Stitching Architecture for Continuous Full Flight-Envelope Simulation of Fixed-Wing Aircraft and Rotorcraft from Discrete Point Linear Models," TR, 2016, https://apps.dtic.mil/sti/citations/AD1008448.

[52] Berger, T., Tischler, M. B., Hagerott, S. G., Cotting, M. C., and Gray, W. R., "Identification of a Full-Envelope Learjet-25 Simulation Model Using a Stitching Architecture," *Journal of Guidance, Control, and Dynamics*, Vol. 43, No. 11, 2020, pp. 2091–2111.
https://doi.org/10.2514/1.G005094

[53] de Boor, C., "B-Form Basics," *Geometric Modeling: Algorithms and New Trends*, edited by G. Farin, SIAM, Philadelphia, PA, 1987, pp. 131–148.

[54] Lai, M. J., and Schumaker, L. L., *Spline Functions on Triangulations*, Cambridge Univ. Press, Cambridge, England, U.K., 2007.
https://doi.org/10.1017/CBO9780511721588

[55] Hu, X. L., Han, D. F., and Lai, M. J., "Bivariate Splines of Various Degrees for Numerical Solution of Partial Differential Equations," *SIAM Journal on Scientific Computing*, Vol. 29, No. 3, 2007, pp. 1338–1354.

[56] Farin, G., "Triangular Bernstein-Bézier Patches," *Computer Aided Geometric Design*, Vol. 3, No. 2, 1986, pp. 83–127.

[57] Lai, M. J., "Geometric Interpretation of Smoothness Conditions of Triangular Polynomial Patches," *Computer Aided Geometric Design*, Vol. 14, No. 2, 1997, pp. 191–199.

[58] de Visser, C. C., Brunner, E., and Verhaegen, M., "On Distributed Wavefront Reconstruction for Large-Scale Adaptive Optics Systems," *Journal of the Optical Society of America A: Optics, Image Science, and Vision*, Vol. 33, No. 5, 2016, pp. 817–831.
https://doi.org/10.1364/JOSAA.33.000817

[59] Kuhn, H. W., "Some Combinatorial Lemmas in Topology," *IBM Journal of Research and Development*, Vol. 4, No. 5, 1960, pp. 518–524.
https://doi.org/10.1147/RD.45.0518

[60] Bey, J., "Simplicial Grid Refinement: On Freudenthal's Algorithm and the Optimal Number of Congruence Classes," *Numerische Mathematik*, Vol. 85, No. 1, 2000, pp. 1–29.
https://doi.org/10.1007/S002110050475

[61] Awanou, G., Lai, M. J., and Wenston, P., "The Multivariate Spline Method for Scattered Data Fitting and Numerical Solutions of Partial Differential Equations," *Wavelets and Splines*, edited by G. Chen, and M. J. Lai, Nashboro Press, Brentwood, TN, 2005, pp. 24–75.

[62] de Visser, C. C., Chu, Q. P., and Mulder, J. A., "Differential Constraints for Bounded Recursive Identification with Multivariate Splines," *Automatica*, Vol. 47, No. 9, 2011, pp. 2059–2066.

[63] Tol, H. J., de Visser, C. C., and Kotsonis, M., "Model Reduction of Parabolic PDEs Using Multivariate Splines," *International Journal of Control*, Vol. 92, No. 1, 2019, pp. 175–190.
https://doi.org/10.1080/00207179.2016.1222554

[64] Hoerl, A. E., and Kennard, R. W., "Ridge Regression: Biased Estimation for Nonorthogonal Problems," *Technometrics*, Vol. 42, No. 1, 2000, p. 80. https://doi.org/10.2307/1271436

[65] Awanou, G., and Lai, M. J., "On the Convergence Rate of the Augmented Lagrangian Algorithm for Nonsymmetric Saddle Point Problems," *Applied Numerical Mathematics*, Vol. 54, No. 2, 2005, pp. 122–134.

[66] Sun, L. G., de Visser, C. C., Chu, Q. P., and Mulder, J. A., "Online Aerodynamic Model Identification Using a Recursive Sequential Method for Multivariate Splines," *Journal of Guidance, Control, and Dynamics*, Vol. 36, No. 5, 2013, pp. 1278–1288. https://doi.org/10.2514/1.60375

[67] Brunner, E., de Visser, C., Vuik, C., and Verhaegen, M., "GPU Implementation for Spline-Based Wavefront Reconstruction," *Journal of the Optical Society of America A: Optics, Image Science, and Vision*, Vol. 35, No. 6, 2018, pp. 859–872. https://doi.org/10.1364/JOSAA.35.000859

[68] Deng, W., Lai, M. J., Peng, Z., and Yin, W., "Parallel Multi-Block ADMM with $o(1/k)$ Convergence," *Journal of Scientific Computing*, Vol. 71, No. 2, 2017, pp. 712–736. https://doi.org/10.1007/s10915-016-0318-2

[69] Bertsekas, D. P., and Tsitsiklis, J. N. J., *Parallel and Distributed Computation: Numerical Methods*, Athena Scientific, Belmont, MA, 1989, http://scholar.google.com/scholar?hl=en&btnG=Search&q=intitle:parallel+and+distributed+computation:+numerical+methods#2.

[70] Rao, C. R., *Linear Statistical Inference and Its Applications*, Wiley, Hoboken, NJ, 2002.

[71] Kariya, T., and Kurata, H., *Generalized Least Squares*, Wiley, Hoboken, NJ, 2004.

[72] Klein, V., and Morelli, E. A., *Aircraft System Identification: Theory and Practice*, AIAA, Reston, VA, 2006.

[73] Niestroy, M. A., Dorsett, K. M., and Markstein, K., "A Tailless Fighter Aircraft Model for Control-Related Research and Development," *AIAA Modeling and Simulation Technologies Conference*, AIAA Paper 2017-1757, Jan. 2017. https://doi.org/10.2514/6.2017-1757

[74] Mulder, M., Lubbers, B., Zaal, P. M. T., van Paassen, M. M., and Mulder, J. A., "Aerodynamic Hinge Moment Coefficient Estimation Using Automatic Fly-by-Wire Control Inputs," *AIAA Modeling and Simulation Technologies Conference and Exhibit*, AIAA Paper 2009-5692, Aug. 2009.

[75] Scholten, P. A., van Paassen, M. M., Chu, Q. P., and Mulder, M., "Variable Stability In-Flight Simulation System Based on Existing Autopilot Hardware," *Journal of Guidance, Control, and Dynamics*, Vol. 43, No. 12, 2020, pp. 2275–2288. https://doi.org/10.2514/1.G005066

[76] Dorsett, K. M., and Mehl, D. R., "Innovative Control Effectors (ICE) Phase I," U.S. Air Force Research Lab. WL-TR-96-3043, 1996.

[77] Dorsett, K. M., Fears, S. P., and Houlden, H. P., "Innovative Control Effectors (ICE) Phase II," U.S. Air Force Research Lab. WL-TR-97-3059, 1997.

[78] Dias, J. N., "High Angle of Attack Model Identification with Compressibility Effects," *AIAA Atmospheric Flight Mechanics Conference*, AIAA Paper 2015-1477, Jan. 2015, pp. 1–15. https://doi.org/10.2514/6.2015-1477

[79] Tol, H., de Visser, C., van Kampen, E., and Chu, Q., "Nonlinear Multivariate Spline-Based Control Allocation for High-Performance Aircraft," *Journal of Guidance, Control, and Dynamics*, Vol. 37, No. 6, 2014, pp. 1840–1862. https://doi.org/10.2514/1.G000065

[80] Sieberling, S., Chu, Q. P., and Mulder, J. A., "Robust Flight Control Using Incremental Nonlinear Dynamic Inversion and Angular Acceleration Prediction," *Journal of Guidance, Control, and Dynamics*, Vol. 33, No. 6, 2010, pp. 1732–1742.

[81] Wang, X., van Kampen, E. J., Chu, Q., and Lu, P., "Stability Analysis for Incremental Nonlinear Dynamic Inversion Control," *Journal of Guidance, Control, and Dynamics*, Vol. 42, No. 5, 2019, pp. 1116–1129. https://doi.org/10.2514/1.G003791

[82] Härkegård, O., "Efficient Active Set Algorithms for Solving Constrained Least Squares Problems in Aircraft Control Allocation," *Proceedings of the 41st IEEE Conference on Decision and Control*, Vol. 2, 2002, pp. 1295–1300. https://doi.org/10.1109/CDC.2002.1184694

[83] Anon., "Notice of Proposed Amendment 2015-13: Loss of Control Prevention and Recovery Training," European Aviation Safety Agency TR NPA 2015-13, 2015.

[84] Anon., "Advisory Circular—Subject: Upset Prevention and Recovery Training (AC 120-111)," Federal Aviation Administration TR AC 120-111, 2017.

[85] Schroeder, J. A., Bürki-Cohen, J., Shikany, D. A., Gingras, D. R., and Desrochers, P., "An Evaluation of Several Stall Models for Commercial Transport Training," *AIAA Modeling and Simulation Technologies Conference*, AIAA Paper 2014-1002, Jan. 2014. https://doi.org/10.2514/6.2014-1002